International Journal of Heat and Mass Transfer 120 (2018) 267–283

Contents lists available at ScienceDirect

International Journal of Heat and Mass Transfer

journal homepage: www.elsevier.com/locate/ijhmt

LBM simulation of unsteady flow and heat transfer from a diamond-shaped porous cylinder

T.R. Vijaybabu, K. Anirudh, S. Dhinakaran *

The Centre for Fluid Dynamics, Discipline of Mechanical Engineering, Indian Institute of Technology Indore, Simrol, Indore 453552, India

ARTICLE INFO

Article history:
Received 16 April 2017
Received in revised form 3 November 2017
Accepted 3 November 2017
Available online 18 December 2017

Keywords:
Darcy-Forchheimer force term
D2Q9 model
LBM
Porous diamond-shaped cylinder
Vortex suppression
Wake suppression

ABSTRACT

Incompressible, two-dimensional unsteady flow and heat transfer around a permeable diamond-shaped cylinder placed in an infinite stream of fluid have been numerically analyzed employing D2Q9 lattice model of the lattice Boltzmann method. The variations in hydrodynamic and thermal behaviour of the permeable diamond cylinder have been studied for different values of Darcy numbers ($10^{-6} \leqslant Da \leqslant 10^{-2}$) and Reynolds numbers ($50 \leqslant Re \leqslant 150$). The force term which comprises the effects of linear and nonlinear drag forces of the porous medium (the Darcy-Forchheimer term) is directly coupled with collision equation for flow through the porous zone. Single relaxation parameter (SRT-BGK collision operator) is used to relax the particles towards equilibrium. A comprehensive analysis of the effects of *Re* and *Da* values on vortex suppression and wake depletion is presented. In addition, the influence of permeability on thermal enhancement ratio at different surfaces of the porous diamond-shaped cylinder is elucidated. A substantial reduction in vortex strength is witnessed for the same *Re* with higher permeability. Reduction in drag, suppression of vortex shedding and heat transfer augmentation are seen in the permeably rich cylinder. Correlations for time-averaged mean Nusselt number, valid for the range of parameters considered in the present study, are also provided. Furthermore, a comparative study on thermal dissipation from the permeable square and diamond shaped cylinders is carried out at $Re = 50$, 100 and 150 at different values of *Da*. This analogy sheds light on understanding the effect of porous body orientation on heat transfer enrichment, which may be handy while modeling porous medium for different engineering applications.

1. Introduction

The remarkable growth in miniaturisation and performance of electronic devices and the increasing use of Multi-Chip-Module (MCM), demands reliable thermal control methods. The conventional thermal control techniques such as natural and forced convection are not sufficient in many cases to meet cooling requirements. Consequently, along with these methods, some other cooling practices with minimum frictional losses have also been developed. And amongst these cooling schemes, one of the promising practices is the use of porous medium. Apart from electronic cooling, porous medium has also been applied in diverse collection of technological applications. Some of these applications include design of chemical nuclear biological filters [1], modeling of heat exchanger, cooling towers, antennas, electronic devices [2], design of air frames [3], flow system in a bioreactor with porous scaffold [4] and fluid flow relative to porous particles in a fluidized bed [5]. As a result, numerous flow and heat transfer studies around porous medium have been carried out both numerically and experimentally on idealised configurations. Such configurations with the information of coefficient of drag and lift, wake length and Nusselt number serve as a launching pad for modeling transport phenomenon in real time systems.

Early investigations done by Poulikakos and Kazmierczak [6] and Chikh et al. [7] suggest that to enhance heat transfer performance of a heated channel, it is not necessary to fill the channel completely with porous medium. Furthermore, Chikh et al. [7] have reported that the heat transfer can be augmented systematically even at low permeability values by using highly conductive porous material. Later, Sung [8] has elucidated the significance of porous blocks on heat dissipation enhancement. Owing to the several applications and heat evacuation ability of porous media, the flow and heat transfer characteristics of porous bluff bodies have been discussed by several researchers for various condition of permeability, porosity, Reynolds number and shapes. Yu et al. [9] performed a numerical analysis on wake structure behind a permeable square cylinder. Their study shows that the size and location of the

* Corresponding author.
E-mail addresses: sdhina@iiti.ac.in, ssdhinakar@gmail.com (S. Dhinakaran).

https://doi.org/10.1016/j.ijheatmasstransfer.2017.11.010
0017-9310/

Nomenclature

Notations

C_1&C_2	binary constants
c_F	non-dimensional Forchheimer term
c_s	speed of the sound, [ms^{-1}]
d_p	particle diameter, [m]
F	body force due to the presence of the porous medium, [N]
F_r	resultant force acting on the cylinder, [N]
F_y	lift force, [N]
H	characteristic height of the cylinder [m]
L_D	downstream length
Ma	Mach number, $\frac{u}{c_s}$
M_i^{eq}	equilibrium distribution function of temperature in direction i
N_i^{eq}	equilibrium distribution function of density in direction i
Nu	local Nusselt number, $\frac{\partial\theta}{\partial n}$
Pr	Prandtl number, $\frac{\nu}{\alpha}$
R_k	thermal conductivity ratio, $\frac{k_e}{k}$
u	non-dimensional x-component velocity, [ms^{-1}]
V	auxiliary velocity, [ms^{-1}]
x, y	horizontal & vertical coordinate
C_D	coefficient of drag, $\frac{F_x}{0.5\rho u_0^2}$
C_L	coefficient of lift, $\frac{F_y}{0.5\rho u_0^2}$
Da	Darcy number, $\frac{K}{H^2}$
$\vec{e}_i$	discrete lattice velocity in direction i, $\frac{\Delta x_i}{\Delta t}$
F_i	total force term due to porous medium, [N]
F_x	drag force, [N]
G	body force due to gravity [N]
K	permeability of the material, [m^2]
L_U	upstream length
M_i	temperature distribution function in direction i
N_i	particle density distribution function in direction i
N	number of lattices on the cylinder
p	dimensionless pressure, $\frac{p^*}{\rho u_\infty^2}$
Re	Reynolds number, $\frac{u_\infty H}{\nu}$
T	dimensional temperature, [°C]
v	non-dimensional y-component velocity, [ms^{-1}]
w_i	weighing factor in direction i

Greek symbols

ρ	fluid density, [kg m^{-3}]
τ'	dimensionless relaxation time for temperature
Δt	time step [s]
θ	dimensionless temperature, $\frac{T-T_\infty}{T_w-T_\infty}$
ν	fluid kinematic viscosity, [m^2 s^{-1}]
Λ	viscosity ratio, $\frac{\mu_e}{\mu}$
τ	dimensionless relaxation time for density
τ_t	non-dimensional time, $\frac{tu_\infty}{H}$
Δx	lattice space
ϵ	porosity
μ	fluid dynamic viscosity, [N s m^{-2}]
α	thermal diffusivity, [m^2 s^{-1}]

Subscripts

∞	far field value
M	mean value
w	wall
BC	rear top slant edge of the cylinder
DA	front bottom slant edge of the cylinder
o	inlet value
i	lattice link direction
AB	front top slant edge of the cylinder
CD	rear bottom slant edge of the cylinder
e	effective

Superscripts

$*$	dimensional form of variables

recirculating wake mainly depend on *Re* and *Da*. Furthermore, it is observed that due to the penetration of fluid at higher *Da*, convection rate of vorticity increases. Jue [10] analysed the vortex shedding behind a porous square cylinder using finite element method. Author has described the effects of permeability on Strouhal number, drag and lift coefficients at *Re* = 100, 200 and 250 with *Da*=10^{-5} to 10^{-4}. Their results show that vortex shedding occurs early with longer shedding period for flow past a low permeable cylinder. Chen et al. [11] presented the flow configurations of porous square cylinder for *Da* from 10^{-5} to 10^{-2} and *Re* from 2 to 250. Their study indicates that at higher permeability, the fluctuation-amplitude of drag coefficient increases. This implies that the square porous cylinder would exhibit longer vortex shedding period with higher amplitude. However, in general, a more porous body should reduce the intensity of vortex shedding. To further understand this phenomenon on other shapes of porous body would be interesting. From the above discussion, it is clear that permeability strongly influences wake length, flow separation point, and vortex shedding phenomena for the flow across a porous square cylinder. These studies imply that porous material plays an important role in flow regularization and stability of structures.

Analysis made by Dhinakaran and Ponmozhi [2] on a heated permeable square cylinder reveals that the increase in permeability reduces the drag coefficient as well as delays the flow separation. Also, this steady flow investigation lightened that the permeable cylinder has higher heat transfer rate compared to a solid cylinder. Wu and Wang [12] numerically examined the features of laminar flow across a porous square cylinder placed in middle of the channel, with heated bottom surface. They have reported that the maximum increase in time-mean average Nusselt number is 107% at $Da = 10^{-2}$ and *Re* = 700. This finite element study also reveals that the cylinder with rich porous properties generates a shorter length of wake flow than cylinder with inferior porous properties. Fu et al. [13] studied numerically on thermal enhancement in laminar channel flow with a porous block in it. They have examined the effects of channel confinement, solid boundary placement and flow inertia on thermal performance of a heated wall. The studies related to heat transfer from porous media suggest that the heat dissipation rate can be elevated by increasing the permeability and other flow governing parameters. For instance, in pin-fin arrangement, which is used as a passive way to increase heat transfer, the arrangement of the fins can be changed to obtain higher permeability and hence, better thermal performance. Instead of modeling individual fins to build the entire pin fin arrangement, one can go for the simplification of modeling a resembling porous bluff body, so as to achieve the bifold goal of reduction in computational complexity and cost. And the same is graphically well-explained through Fig. 1(a).

Several studies [14–18] have also testified the effects of incident angle of a square cylinder on wake structure, drag, lift and vortex shedding. Especially, the detailed numerical evaluation performed by Yoon et al. [14] elucidates the flow characteristics for the flow across solid square cylinder, inclined with respect to the main flow in laminar flow regime. They have reported that the variation in

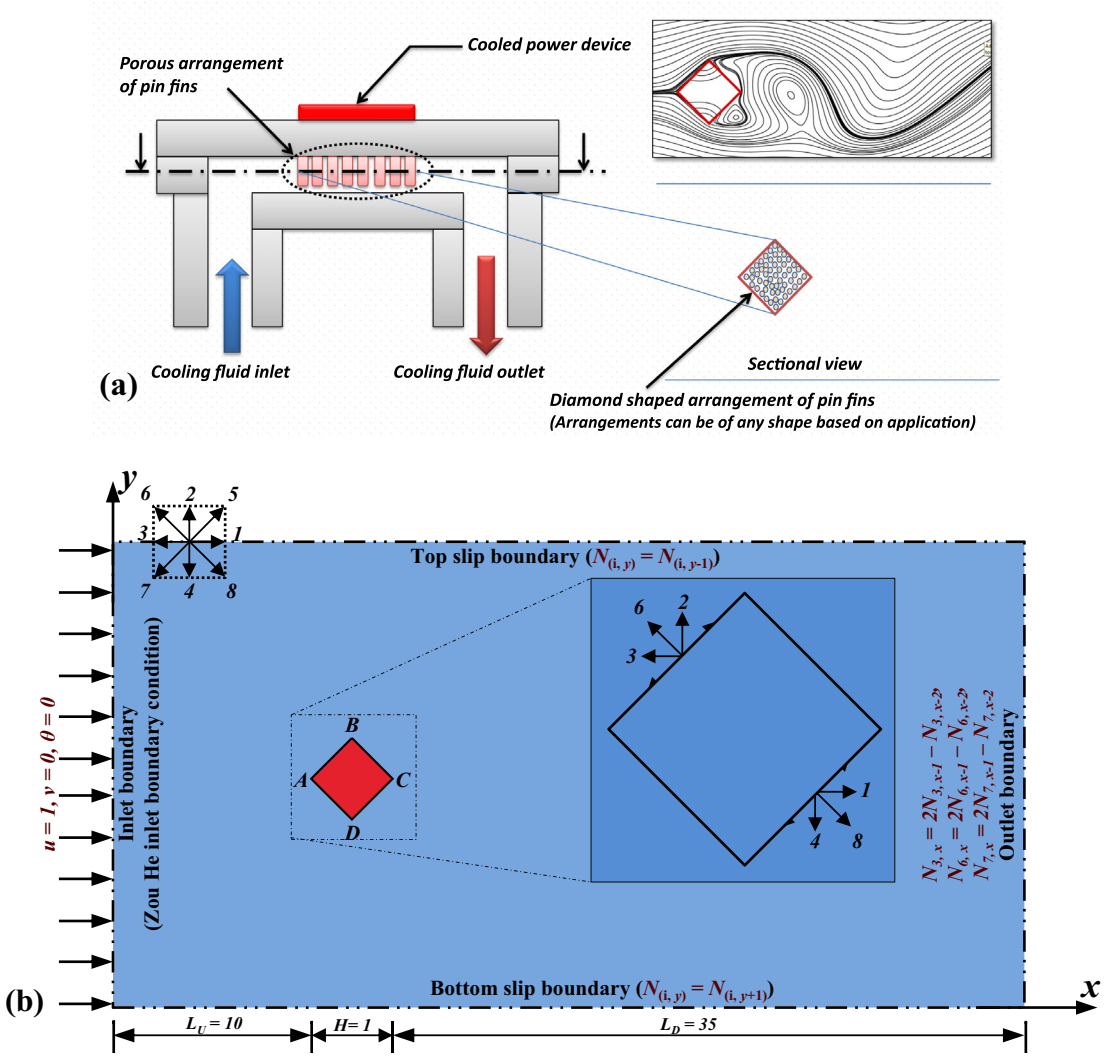

Fig. 1. (a) A simple sketch of flow around diamond-shaped porous arrangements of pin-fins which imitate the scenario of flow around and through diamond-shaped porous body; (b) computational domain for the unconfined flow and heat transfer from a porous diamond-shaped cylinder.

recirculating wake is low for both steady and unsteady cases at incidence angle, $\theta = 45^\circ$ (i.e. diamond shape). Also, diamond-shaped bluff body shows zero mean pressure lift coefficients for all the considered values of *Re*. This indicates that the square body with 45° incident angle will have less stability issues in unsteady flow. Hence, the flow characteristics of diamond-shaped body will be more interesting to look into under different permeability conditions. Although several studies are available on permeable square cylinder, only a few of them are based on diamond-shaped cylinder. Analysis of fluid flow around and through a porous diamond-square cylinder made by Valipour et al. [19] explore the effects of *Da* and *Re* on pressure coefficient, wake structure and streamlines. Their numerical study shows that due to different shapes of forebodies and afterbodies, the critical *Re* for onset of wake for a square cylinder is smaller than that of the diamond-square cylinder. Rashidi et al. [20] examined steady, laminar and two-dimensional flow around and through a porous diamond cylinder with apex angles, 15°, 30°, 45° and 60°. They have found that at higher apex angles, the wake detaches from the cylinder due to the increase in fluid momentum from cylinder to fluid zones. Rashidi et al. [21] numerically studied the flow and forced convective heat transfer around and through a diamond-shaped porous cylinder for *Re* = 1–45, $Da = 10^{-6}$ - 10^{-2} with a constant porosity value of 0.5. They have employed finite volume method and Darcy-Forchheimer equation in the porous zone. It is reported that the size of thermal cloud is increasing with the increase of *Da* and *Re*. It can be seen that at $Da = 10^{-6}$ and *Re* = 40, the mean Nusselt number of the diamond cylinder is around 3.3, whereas, at same hydrodynamic conditions, the mean Nusselt of the permeable square cylinder is 2.67 (heat transfer enhancement of 19%) [2]. It is very clear that rich heat transfer characteristics can be obtained if the incident angle of flow to the cylinder becomes 45°. With this perspective, we propose to study the effects of using an isolated porous diamond shaped cylinder in a uniform flow of air. A review of available literature show that the forced convection heat transfer from an isolated permeable diamond shaped cylinder in the laminar unsteady flow regime has not yet been conducted. Besides, there are no results available on vortex shedding phenomenon, drag coefficient and heat transfer characteristics of porous diamond shaped cylinder with different permeability which are important parameters to be considered.

For past three decades, lattice Boltzmann method (LBM) has been serving as a pretty matured alternative technique for solving transport and isothermal problems. Also, it has proven its ability while dealing with complex geometry, flow through porous media, chemical reactions, and multiphase flow. While solving incom-

pressible flows, due to pressure term in the Navier-Stokes equation, the traditional CFD methods consume more time. Especially, for unsteady problems, solving the Laplace equation to satisfy continuity equation at each time step requires more computational resources [22]. In case of LBM, there is no need of such process due to its kinetic approach. Mohebbi et al. [23] have compared lattice Boltzmann method with finite element method for the power-law fluid flow and heat transfer over a heated square cylinder placed in a channel. It is reported that the LBM consumes less memory in comparison to FEM, about 1/8 times less. Further, it is stated that the computational time of LBM is much lesser than that of FEM. Regulski and Szumbarski [18] analysed a series of benchmark two-dimensional simulations using LBM to assess the impact of grid refinement on results of the simulations. They have considered time dependent flows past a circular and diamond-shaped cylinder confined in a channel with parallel plates. The stair-case form of geometry makes it possible to appropriately reproduce shapes other than horizontal and vertical walls. Though methods incorporating curvilinear geometry to the LBM simulation [24,25] exist, their study concentrates on issues related to surface roughness due to stair-case geometry on flow. They have shown that the half-way bounce-back method turns out to be sufficient and effects of stair-case do not play any significant role. However, the number of lattices on the cylinder should be sufficiently fine to avoid the raster effects on boundaries. Nazari et al. [26] have used LBM to investigate the heat transfer enhancement in a channel partially filled with an anisotropic porous block. The results of pore scale simulation show that the heat transfer primarily depends on the obstacle arrangement, blockage ratio, *Re* and porosity. They have imposed bounce-back boundary condition on solid obstacles of the porous block. Later, Nazari et al. [27] have performed a similar study using power-law fluids. They have reported that the random arrangement of square obstacles in the porous block delivers rich thermal performances than regular arrangement. To enable LBM at REV scale porous medium flow, Guo and Zhao [28] applied a force term that accounts for the drag effects due to the presence the porous medium. Later, Guo and Zhao [29] proposed an LB model for convection heat transfer in porous media. A separate distribution function is used in this model and also, they have derived a macroscopic equation for convection heat transfer in porous media by the Chapman-Enskog procedure. Babu and Narasimhan [30] applied LBM to investigate the vortex shedding behind a porous square cylinder. They have used second order Lagrangian interpolation after the streaming process, to simulate the flow in a nonuniform computational grid. D2Q9i lattice model, which has the ability to recover Navier-Stokes equation from the LB equation within $O(Ma^2)$ is used in their investigation. More recently, Vijaybabu et al. [31] have investigated mixed convection heat transfer from a square-shaped permeable cylinder using LBM. Apart from these kinds of literature, other studies [32–37] also show the potential of LBM in modeling flow in unsteady flow regime and through porous medium. By considering this advantage we have employed lattice Boltzmann technique in our study.

The porous bluff body or arrangement of body resembling porous structure is encountered in various applications such as porous heat sink, pin-fin arrangements and LED back-light module. The miniaturization of electronic components requires these thermal dissipation devices as tiny in size. On such instances, the shear layer produced by the boundary does not affect much on flow and heat transfer behaviour of aforementioned applications. Hence, a significant amount of knowledge is essential to model such thermal systems for maximum heat transfer while it is far from boundary. From the literature it is clear that the hydrodynamic and thermal phenomenon of a heated porous diamond-shaped cylinder in unsteady regime has not been addressed yet. The prime objective of the present study is to analyze the influence of permeability on flow and heat transfer traits of an isolated porous-diamond shaped cylinder in unsteady regime using LBM. A force term which accounts for drag effects due to porous media (Darcy-Forchheimer) is explicitly coupled with the collision equation of flow. Also, for convection heat transfer in porous media, a separate distribution function is added as suggested by Guo and Zhao [29].

2. Mathematical formulation

2.1. Problem description

Schematic of the computational setup under investigation is shown in Fig. 1(b). A fixed 2D diamond-shaped cylinder of height, H is placed inside a rectangular domain, whose boundaries are far away from the permeable cylinder. The cylinder, which is placed in a fluid flow with free stream velocity u_∞ and temperature T_∞, is maintained at a constant temperature T_w ($T_w > T_\infty$). In order to simplify the problem and make it amenable for the numerical simulations, the following assumptions were made:

(i) The flow is laminar, two-dimensional and incompressible. The fluid flows around and through an isotropic, homogeneous porous body. Porosity and permeability in the porous zone are uniform.
(ii) Properties of the fluid are considered to be constant and the body forces are neglected in this study. There is no internal heat generation in the porous body and the viscous dissipation inside the porous zone is negligible.
(iii) In porous zone, the fluid phase and solid phase temperature are considered to be equal (LTE - Local Thermal Equilibrium). This assumption will not hold good in the case of rapid cooling/heating or problem with significant temperature difference between fluid and solid phase in porous region [38].

2.2. Conservation equations

Considering above assumptions, the following non-dimensional governing equations are used to represent flow and heat transfer phenomena [2].

$$\frac{\partial u}{\partial x}+\frac{\partial v}{\partial y}=0. \tag{1}$$

$$\frac{\partial u}{\partial \tau_t}+\frac{1}{\epsilon}\left(u\frac{\partial u}{\partial x}+v\frac{\partial u}{\partial y}\right)=-\epsilon\frac{\partial p}{\partial x}+\frac{\Lambda}{Re}\left(\frac{\partial^2 u}{\partial x^2}+\frac{\partial^2 u}{\partial y^2}\right) - C_1\epsilon\frac{1}{ReDa}u-C_2\frac{1.75}{\sqrt{150}}\frac{1}{\sqrt{Da}} \times\frac{\sqrt{u^2+v^2}}{\sqrt{\epsilon}}u. \tag{2}$$

$$\frac{\partial v}{\partial \tau_t}+\frac{1}{\epsilon}\left(u\frac{\partial v}{\partial x}+v\frac{\partial v}{\partial y}\right)=-\epsilon\frac{\partial p}{\partial y}+\frac{\Lambda}{Re}\left(\frac{\partial^2 v}{\partial x^2}+\frac{\partial^2 v}{\partial y^2}\right) - C_1\epsilon\frac{1}{ReDa}v-C_2\frac{1.75}{\sqrt{150}}\frac{1}{\sqrt{Da}} \times\frac{\sqrt{u^2+v^2}}{\sqrt{\epsilon}}v. \tag{3}$$

$$\frac{\partial \theta}{\partial \tau_t}+\frac{1}{\epsilon}\left(u\frac{\partial \theta}{\partial x}+v\frac{\partial \theta}{\partial y}\right)=\frac{R_k}{Re\cdot Pr}\left(\frac{\partial^2 \theta}{\partial x^2}+\frac{\partial^2 \theta}{\partial y^2}\right). \tag{4}$$

Here, C_1 and C_2 are the binary constants which hold the value of 0 at clear fluid zone and 1 at the porous zone. The dimensionless variables are defined as: $Re = \rho u_\infty H/\mu$ is the Reynolds number, $Pr = \mu C_p/k$ is the Prandtl number, $\Lambda = \mu_e/\mu$, denotes the viscosity ratio. The viscosity ratio and thermal conductivity ratio are assumed to be unity in the present study. The above non-dimensional governing equations are obtained by introducing the following characteristic scales:

$$x = \frac{x^*}{H}, \quad y = \frac{y^*}{H}, \quad \tau_t = \frac{tu_\infty}{H}, \quad p = \frac{p^*}{\rho u_\infty^2}, \quad u = \frac{u^*}{u_\infty},$$
$$v = \frac{v^*}{v_\infty}, \quad \theta = \frac{T - T_\infty}{T_w - T_\infty}.$$

It is to be noted that the superscript * indicates the dimensional form of the variable.

2.3. Lattice Boltzmann Method (LBM)

Lattice Boltzmann method is a statistical approach for solving transport phenomenon in which the fluid is replaced by fractious particles. Based on the distribution of these grouped particles, macroscopic properties of the fluid are evaluated. These particles stream along the direction defined by the lattice links and collide at lattice site. Due to the collision process, particle distribution changes and accordingly the direction, density, and velocity of the fluid also varies. In traditional CFD, the Laplace equation must be solved at each time step in order to satisfy the continuity equation. Hence, it demands more computational time, especially for unsteady-state problems. Due to the explicit nature of LBM, there is no need for such process. Apart from this, boundary condition implementation in complex region can be easily defined by particle reflection rule. It is well-known that the Navier-Stokes equations are second order PDE, whereas, the governing equations of LBM are of first order. Thus, the discretization and programming of LBM is much simpler than FVM. Furthermore, in comparison to the finite volume method, LBM easily deals with multiphase flows and complex solid-fluid phase such as flow through porous media.

2.3.1. LB governing equations for velocity field

The governing equation of traditional LBM is written in terms of a distribution function. To extend LB equation for the porous media flow, a force term is coupled with the collision operator. The extended LB governing equation [28] can be expressed as

$$N_i(\vec{x} + \vec{e}_i\Delta t, t + \Delta t) - N_i(\vec{x}, t) = -\frac{1}{\tau}[N_i(\vec{x}, t) - N_i^{eq}(\vec{x}, t)] + \Delta t F_i. \tag{5}$$

In Eq. (5), N_i is the instantaneous particle density at a link, N_i^{eq} is the corresponding equilibrium density and e_i is the velocity direction vector of the particles that reside in the lattice. In the present analysis, D2Q9 lattice model has been used in which a rest particle is surrounded by eight different direction particles. Based on the direction, these particles move at each time step with a certain speed. This speed (for the D2Q9 lattice model) can be written as

$$\vec{e}_i = \begin{cases} (0,0), & i = 0 \\ (\cos[(i-1)\pi/2], \sin[(i-1)\pi/2])e, & i = 1-4 \\ (\cos[(2i-9)\pi/4], \sin[(2i-9)\pi/4])\sqrt{2}e, & i = 5-8. \end{cases} \tag{6}$$

BGK collision operator with single relaxation time (SRT) can be seen on the right side of Eq. (5). At each time step of the collision operation, the particles have to be relaxed towards to the equilibrium condition within some relaxation factor (τ) and this value is the same for all the particles that reside in a single lattice in the case of SRT model. The Chapman-Enskog relation relates the LB fluid viscosity and the non-dimensional relaxation time and it can be written as

$$v = \left(\tau - \frac{1}{2}\right)\Delta t c_s^2. \tag{7}$$

In Eq. (5), a force term F_i, which accounts for the drag effects due to the presence of porous medium (porosity-ϵ) is added with the BGK collision operator. This force term is deactivated in clear fluid region. This force term of the porous medium can be written as

$$F_i = w_i\rho\left(1 - \frac{1}{2\tau}\right)\left[3(\vec{e}_i \cdot \vec{F}) + \frac{9}{\epsilon}(\vec{e}_i \cdot \vec{U})(\vec{e}_i \cdot \vec{F}) - \frac{3}{\epsilon}(\vec{U} \cdot \vec{F})\right]. \tag{8}$$

In the above equation, $\vec{F}$ is the Darcy-Forchheimer force or body force due to the presence of porous medium, which considers both viscous and inertial force, and it can be written as

$$\vec{F} = -\frac{\epsilon v}{K}\vec{U} - \frac{\epsilon c_F}{\sqrt{K}}|\vec{U}|\vec{U} + \epsilon G. \tag{9}$$

Here, v is the kinematic viscosity of the fluid, K is permeability of the porous medium, $c_F = 1.75/\sqrt{150 \times \epsilon}$, is the nondimensional Forchheimer form, $|\vec{U}| = \sqrt{u^2 + v^2}$ in which u and v are the components of $\vec{U}$ in x and y - directions respectively, and G is the body force due to gravity. The updated equilibrium distribution function with porosity term can be written as

$$N_i^{eq} = w_i\rho\left[1 + 3(\vec{e}_i \cdot \vec{U}) + \frac{9}{2\epsilon}(\vec{e}_i \cdot \vec{U})^2 - \frac{3}{2\epsilon}(\vec{U} \cdot \vec{U})\right], \tag{10}$$

where w_i is the weighing factor of each lattice link in the lattice arrangement. For D2Q9 model, the weighing factors are $w_0 = 4/9$, $w_i = 1/9$ for $i = 1, 2, 3, 4$ and $w_i = 1/36$ for $i = 5, 6, 7, 8$. Once after performing mesoscopic level collision, streaming, and appropriate boundary conditions, the macroscopic properties need to be evaluated. The sum of distribution functions of a lattice at each point represents the density of fluid at that point. Therefore, the density (ρ) and velocity ($\vec{U}$) of fluid can be calculated from the distributions data and it can be written as

$$\rho = \sum_{i=0}^{8} N_i. \tag{11}$$

$$\rho\vec{V} = \sum_{i=1}^{8} \vec{e}_i N_i + \frac{\Delta t}{2}\rho\vec{F}. \tag{12}$$

Here, V is the auxiliary velocity in case of porous medium and the actual velocity at this region can be calculated from the following equation:

$$\vec{U} = \frac{\vec{V}}{c_0 + \sqrt{c_0^2 + c_1|\vec{V}|}}. \tag{13}$$

The two parameters c_0 and c_1 in Eq. (13) are given by

$$c_0 = \frac{1}{2}\left(1 + \epsilon\frac{\Delta t}{2}\frac{v}{K}\right); \quad c_1 = \epsilon\frac{\Delta t}{2}\frac{c_F}{\sqrt{K}}. \tag{14}$$

2.3.2. LB governing equations for thermal field

In the case of convection heat transfer, the evolution of thermal field is defined by another distribution function, which is written as

$$M_i(\vec{x}+\vec{e}_i\Delta t, t+\Delta t) - M_i(\vec{x},t) = -\frac{1}{\tau'}[M_i(\vec{x},t) - M_i^{eq}(\vec{x},t)]. \quad (15)$$

In the above equation, τ' is the dimensionless relaxation time for thermal field and it is evaluated from thermal diffusion coefficient ($\alpha = v/Pr$). The Chapman-Enskog relationship for thermal relaxation time can be written as

$$\alpha = \left(\tau' - \frac{1}{2}\right)\Delta t c_s^2. \quad (16)$$

The temperature equilibrium distribution function M_i^{eq} in the Eq. (15) can be written as

$$M_i^{eq} = w_i\theta[1 + 3(\vec{e}_i \cdot \vec{U})]. \quad (17)$$

The temperature, θ can be calculated from the distribution function $M(x,t)$ as

$$\theta = \sum_{i=0}^{8} M_i. \quad (18)$$

2.3.3. Boundary conditions

In traditional CFD techniques, the boundary conditions are defined in terms of macroscopic fluid properties such as density, velocity, and temperature. Lattice Boltzmann simulations carry only the information of particle distribution and hence, the boundary conditions also need to be described in terms distribution functions. Various boundary conditions that are applied in this analysis are described below.

2.3.3.1. Inlet boundary condition. The initial velocity has to be chosen such that Mach number, *Ma* should be less than 0.1 due to weakly compressible nature of LB [22]. A free uniform velocity (u_∞ or u_0) which has lesser compressibility effects is given to the inlet. The distribution functions N_1, N_5 and N_7 fall inside the domain at the inlet region. The Zou and He boundary condition [39] is applied to the inlet of the domain to find out the unknown distribution functions and it can be written as follows:

$$\rho_0 = \frac{1}{1-u_0}[N_0 + N_2 + N_4 + 2(N_3 + N_6 + N_7)]. \quad (19)$$

$$N_1 = N_3 + \frac{2}{3}\rho_0 u_0, \quad N_5 = N_7 + \frac{1}{6}\rho_0 u_0, \quad N_8 = N_6 + \frac{1}{6}\rho_0 u_0. \quad (20)$$

In the above equation, ρ_0 and u_0 are the initial density and velocity (in *x*-direction), respectively.

2.3.3.2. Top and bottom boundary. The study aims to simulate the flow around and through the diamond cylinder in the unconfined domain. Artificial top and bottom boundaries are placed far away from the cylinder in order to avoid the shear stress developed by the boundaries. Therefore, the slip boundary condition needs to be adopted to reach this requirement. The velocity gradients normal to the flow direction at top and bottom boundaries should become zero in order to avoid viscous effects of it. The gradient can be turned to zero by equating the distribution function values of wall to its neighbouring lattice values. The boundary condition can be specified as, $N_{i,y} = N_{i,y-1}$ for the top wall and $N_{i,y} = N_{i,y+1}$ for the bottom wall, where '*i*' is the lattice link direction of D2Q9 arrangement. Furthermore, the adiabatic boundary condition (i.e. $\partial\theta/\partial y = 0$) is imposed on top and bottom boundaries of the computational domain. In LBM, the corresponding boundary condition for top boundary can be written as, $M_{i,y} = M_{i,y-1}$ for the top wall and $M_{i,y} = M_{i,y+1}$ for the bottom wall.

2.3.3.3. Outlet boundary condition. In the present study, we have applied open boundary condition at the outlet of the computational domain. In macroscopic scale this indicates that the velocity and temperature gradients in the flow direction are zero. At outlet, the distribution functions N_3, N_6 and N_7, cannot be evaluated through streaming process, and thus, these distribution functions are evaluated through extrapolation method. It is to be noted that such boundary condition is applied where the outlet velocity is unknown [22]. The thermal boundary conditions at outlet are also specified in similar fashion. Thus, the unknown distribution functions (both flow and thermal) at outlet using second order polynomial can be written as

$$\begin{aligned} N_{3,x} &= 2N_{3,x-1} - N_{3,x-2}; \quad M_{3,x} = 2M_{3,x-1} - M_{3,x-2} \\ N_{6,x} &= 2N_{6,x-1} - N_{6,x-2}; \quad M_{6,x} = 2M_{6,x-1} - M_{6,x-2} \\ N_{7,x} &= 2N_{7,x-1} - N_{7,x-2}; \quad M_{7,x} = 2M_{7,x-1} - M_{7,x-2}. \end{aligned} \quad (21)$$

2.3.3.4. Boundary conditions at porous zone. The force term F_i, which appears in Eq. (5) is enabled at those grid points which falls inside the diamond-shaped porous region. The slant edges of the cylinder pass through vertices of each lattice on the path such that they act as diagonal and hence, no separate boundary treatment is necessary. Therefore, the necessary accuracy can be achieved even with Cartesian grid. Moreover, the body fitted grid requires the interpolation step after streaming operation and thus, the simulation results rely on accuracy of the interpolation. However, the number of grids should be sufficiently large enough to avoid the staircase effects offered by the slant edges. In the present code, the activation of F_i term is governed by a dummy array called $w(i,j)$. Initially, this array is fixed as zero in the whole computational domain. Meanwhile, this array is switched to an integer value of 1 at those grid points which fall inside the porous zone. This can be done by using the expression, $|x| + |y| = H/2$, where, *x* and *y* are the coordinate or grid points in the computational domain. Furthermore, the non-dimensional temperature value of 1 (i.e. $\theta = 1$) is kept in the porous region. In Fig. 1(b), the enlarged view of diamond-shaped cylinder along with lattice placement on slant surfaces is shown. At slant edge *AB*, the lattices N_2, N_3 and N_6 are falling outside of the edge and thus, these distribution functions are need to be specified as $N_2 = \theta(w_2 + w_4) - N_4, N_3 = \theta(w_3 + w_1) - N_1$ and $N_6 = \theta(w_6 + w_8) - N_8$ to fix $\theta = 1$ at this edge. Accordingly, at other slant edges the thermal boundary conditions are imposed.

2.4. Dimensionless parameters

Some of the dimensionless parameters used in this study are defined as follows:

2.4.1. Reynolds number

In LBM, Reynolds number (*Re*) is written in terms of lattice numbers (*N*) as

$$Re = \frac{u_\infty H}{v} = \frac{u_\infty N}{v}, \quad (22)$$

where the height of the cylinder, '*H*' is the characteristic length and the free stream velocity 'u_∞' is the characteristic velocity.

2.4.2. Darcy number

The Darcy number, which represents non-dimensional permeability of the porous body, can be evaluated through the Carman-Kozeny relation [40], in terms of porosity (ϵ) as

$$Da = \frac{1}{180}\frac{\epsilon^3 d_p^2}{H^2(1-\epsilon)^2} = \frac{K}{H^2} = \frac{K}{N^2}. \quad (23)$$

In the present study, we have considered the particle diameter size (d_p) as 1 cm (for $H = 1m$) [41] and with this relationship the porosity value is evaluated for a given value of Darcy number. In LBM, the numerical stability and accuracy of the results mainly depend upon the number of lattices on characteristic length. In the present analysis, N represents the number of lattices that are present on the characteristic height of the cylinder.

2.4.3. Pressure coefficient

The pressure coefficient (C_p) is defined as

$$C_p = \frac{p - p_\infty}{0.5\rho u_\infty}. \tag{24}$$

Here, p and p_∞ are the dimensional pressure on the cylinder surface and far field, respectively. In LBM, the pressure and density are related through the speed of sound (c_s) as $p = c_s^2\rho$. Where, $c_s = e/\sqrt{3}$ in D2Q9 lattice model.

2.4.4. Drag and lift coefficient

The momentum exchange between two opposing directions of neighbouring lattices aids for the evaluation of lift and drag forces. In the current study, the momentum exchange method is employed for the calculation of total resultant force F_r, and it can be written as [42]

$$F_r = \sum_{\text{all}x_b}\sum_{i=1}^{8} e_i\left[\widetilde{N}_i(x_b,t) + \widetilde{N}_i(x_b + e_i\Delta t, t)\right] \times [1 - w(x_b + e_i)]\Delta x/\Delta t. \tag{25}$$

In the above equation, $w(x_b + e_i)$ is an indicator, which is 0 at fluid nodes and 1 at porous nodes. Also, x_b indicates the porous boundary nodes and $\widetilde{N}_i(x_b, t)$ is the post-collision distribution function. For a given non-zero velocity e_i, e_i denotes the lattice velocity in the opposite direction. From the total force, the drag and lift coefficients are calculated as

$$\text{Drag coefficient, } C_D = \frac{F_x}{0.5 \times \rho u_\infty^2 H}. \tag{26}$$

$$\text{Lift coefficient, } C_L = \frac{F_y}{0.5 \times \rho u_\infty^2 H}. \tag{27}$$

Here, F_x and F_y are the x and y-components of the total fluid force acting on the porous cylinder.

2.4.5. Nusselt number

Heat transfer from the permeable cylinder to the flowing fluid can be evaluated through local Nusselt number given by $Nu = -R_k\frac{\partial\theta}{\partial n}$. Here, n is the direction normal to the cylinder surface and R_k is the ratio of thermal conductivity of the porous material (k_e) and fluid (k_f), which is assumed to be unity in this study. Average heat transfer at any face of the permeable body is obtained by taking average of the local Nusselt number along that face. The mean Nusselt number value (Nu_M), which represents the total heat transfer from the permeable cylinder is evaluated from the average Nusselt number of all surfaces as shown below

$$Nu_M = \frac{1}{4}\sum Nu_{AB,BC,CD,DA}. \tag{28}$$

2.4.6. Heat transfer enhancement ratio (E)

The heat transfer augmentation obtained by permeable cylinder with solid cylinder (or permeable cylinder with $Da = 10^{-6}$) is expressed in terms of heat transfer enhancement ratio (E). It is given by the ratio of Nusselt number of any permeable cylinder to Nusselt number of impermeable cylinder ($Da = 10^{-6}$).

$$E = \frac{(Nu)\text{ at any value of } Da}{(Nu)\text{ at } Da = 10^{-6}}. \tag{29}$$

This study has shown the variation of E along different faces of the cylinder and hence, heat transfer enhancement ratio at different faces is represented as E_{AB}, E_{AD}, E_{BC} & E_{CD}.

3. Numerical procedure and validation

3.1. Numerical method

A FORTRAN code has been written on lattice Boltzmann method to conduct present numerical simulations. An LB simulation begins with collision process followed by streaming operation and imposition of boundary conditions and is concluded by evaluation of macroscopic values. Before entering into the main loop of computations, the initialization processes such as evaluation of relaxation times and initial velocity based on Re are carried out. In this study, the BGK collision operator is used, wherein a single non-dimensional relaxation factor (τ) is adopted. The relaxation factors (τ&τ') are calculated from Chapman-Enskog relationship [43]. Initially, the velocities (i.e. u and v) at all nodes are assumed to be zero and the density (ρ) is kept as 1. At inlet boundary, the initial velocity is substituted (i.e. $u = u_0$) and the y-directional velocity at these nodes is kept zero (i.e. $v = 0$). The equilibrium distribution function (N_i^{eq}) which is given in Eq. (10) and porous force term F_i are calculated and these values are substituted in collision equation (i.e. Eq. (5)). The force term appearing in Eq. (5) is applied to the entire computational domain. However, in clear fluid region, this force term is deactivated by multiplying zero and it is enabled in porous zone by multiplying with a constant value of 1. The new distribution function values obtained from the collision process are shifted to the neighbouring lattices based on the lattice direction. Appropriate flow boundary conditions at inlet, top and bottom wall and porous zone are imposed in terms of distribution functions. After defining boundary conditions, the macroscopic properties such as density and velocity are evaluated from Eqs. (11) and (12). At porous zone, the actual porous velocities are calculated from Eqs. (13) and (14). Velocity and density values are then used for the calculation of temperature distribution functions from its collision equation (Eq. (15)). The corresponding thermal boundary conditions are then imposed, followed by the calculation of temperature field at each grid from Eq. (18). New values of density, velocity and temperature are used in the collision equation of flow and the cycle is repeated until the convergence criterion is satisfied. It is seen that the numerical algorithm of lattice Boltzmann is relatively simpler than the conventional CFD methods. In the present work, the LBM computations are carried out till the following convergence criterion is satisfied.

$$\frac{\sqrt{\sum_{i,j}\left[U_{i,j}^{(k+1)} - U_{i,j}^{(k)}\right]^2}}{\sqrt{\sum_{i,j}\left[U_{i,j}^{(k+1)}\right]^2}} \leqslant 10^{-6}, \frac{\sqrt{\sum_{i,j}\left[\theta_{i,j}^{(k+1)} - \theta_{i,j}^{(k)}\right]^2}}{\sqrt{\sum_{i,j}\left[\theta_{i,j}^{(k+1)}\right]^2}} \leqslant 10^{-6}. \tag{30}$$

In the above equation, $U_{i,j}$ is the fluid velocity, $\theta_{i,j}$ is the fluid temperature and k is the iteration level. The results are presented in the form of time-averaged quantities. The average values of velocity and temperature field are calculated for one complete cycle of lift coefficient (C_L). The time-averaged streamline, vorticity and isotherm contours are evaluated from averaged velocity and temperature fields. Also, the drag, pressure and Nusselt number values are averaged for the same one complete cycle of C_L. It is to be noted that the lift coefficient cycle should be selected once after the C_L reaches unsteady periodic nature. The non-dimensional relaxation factors for flow (τ) and thermal (τ') are

taken as 0.56 and 0.5845, respectively. All the calculations have been carried out by using SPARC T4-1 2.85 GHz ORACLE server and the CPU time of each calculation is 3.2 hr with the memory usage of 537 MB.

3.2. Grid and domain independence analysis

The accuracy of LB computation depend on the number of lattices that are present on characteristic distance and variation of the same changes accuracy as well as stability of the simulations. Therefore, the number of lattices (N) present on characteristic height of the cylinder (H) on accuracy is summarized in Tables 1 and 2 along with grid size of the computational domain. The present LB code is tested for 6 different values of N with time-averaged drag coefficient and mean Nusselt number at $Re = 50$ and $Da = 10^{-6}$. The lower lattice numbers on cylinder, produced staircase effect and hence, smaller lattice numbers (i.e. $N \leqslant 38$) have shown large variations in results. This test run indicates that 42 lattice numbers on frontal surface produces less deviation compared to higher values of N at downstream length $L_d = 35H$.

3.3. Code validation

The code used in present study has been validated by comparing our results for $Pr = 0.71$ with the literature related to square and diamond-shaped cylinder of Dhinakaran and Ponmozhi [2], Yoon et al. [14], Rashidi et al. [21], Sharma and Eswaran [44] and Paliwal et al. [45]. The drag coefficient and mean Nusselt number comparison in Fig. 2 shows a variation of 3.2% from the literature results. Tables 3 and 4 compare flow and heat transfer parameters of solid and permeable diamond-shaped cylinder. The observed variations are well within the range and are acceptable. The minor deviation is due to different numerical approaches and discretization methods. It should be noted that the present computations are carried out using mesoscopic approach, whereas the literature considered for comparison uses macroscopic level simulations.

4. Numerical results and discussions

A comprehensive numerical analysis of flow and heat transfer around a permeable diamond-shaped cylinder is presented. The following parameters are employed to study the flow and heat transfer characteristics:

- Reynolds number, $Re = 50$ to 150 in steps of 10.
- Darcy number, $Da = 10^{-6}, 10^{-4}, 10^{-3}$ and 10^{-2}.
- Porosity, $\epsilon = 0.629, 0.935, 0.977, 0.993$ (these values are evaluated from Carman-Kozeny relation, Eq. (23)).
- Prandtl number, $Pr = 0.71$(air).

This numerical study will support us to evaluate the effects of permeability on flow and heat transfer characteristics and the discussion of the results is designated accordingly as follows:

4.1. Flow characteristics

4.1.1. Streamline pattern

The effects of permeability variation on the flow around permeable diamond cylinder is brought out through time-averaged mean flow shown in Fig. 3(a) and (b). In the case of porous medium flow, streamline is a function of Reynolds number and non-dimensional permeability (Da) of the cylinder. The domination of inertial forces over viscous force causes flow separation and as a result of this, regularized twin wakes form behind the cylinder. This twin recirculation wakes develop further while increasing Re and they become asymmetric due to the further increase of inertial forces. In the present study, the flow has been found to be unsteady for the entire range of Reynolds number ($50 \leqslant Re \leqslant 150$) considered. It is seen that the position and size of the vortex are found to be different at different Re and Da. In comparison to instantaneous flow contours, the time-averaged flow patterns provide better pictorial representation of the effects of permeability downstream of the cylinder. Fig. 3(a) and (b) show the streamlines of time-averaged flow at $Re = 50$ and 150, respectively, for various Da values. The time-averaged flow exhibits a twin wake structure behind the cylinder. The reattachment point of the wakes is observed to move towards the cylinder and consequently, the wake length is found to decrease as the Reynolds number is increased. However, the wake width is found to be in direct proportion with Re. Furthermore, for a given Re, the reattachment point of wakes clearly explain that the developed recirculation starts moving away from the cylinder as the non-dimensional permeability values are increased. However, the size of wake structure reduces in both x and y-directions at higher values of permeability due to the lesser restrictions to the flow. In addition to this, the separation point moves away from apex of cylinder with the increase of Da due to higher fluid penetration. At $Da = 10^{-2}$, this wake structure is completely suppressed and fluid penetrates the cylinder with very less deviation. It can also be seen from Fig. 3 that at very low permeability ($Da = 10^{-6}$), almost no fluid penetrates inside the cylinder. Upon increasing Da, fluid starts penetrating inside the cylinder with different deviation levels. This deviation is due to the variation of viscous and inertial terms inside the porous region. Higher viscous drag term in the porous zone obstructs the fluid flow and hence, the deviation is found to be more at lower values of Da values. Further, the inertial forces within the porous region enhances when the cylinder becomes more permeable. Reduction of wake size in time-averaged streamline contours emphasises the influence of permeability on vortex shedding. From the above discussion, it can be discerned that the permeability of the porous diamond-shaped cylinder greatly affects the hydrodynamic characteristics in and around the porous diamond cylinder.

4.1.2. Vorticity pattern

Instantaneous vorticity contours that evolve from the permeable diamond-shaped cylinder is shown in Fig. 4(a) for $Re = 150$ and $Da = 10^{-6}, 10^{-4}, 10^{-3}$ and 10^{-2}. It can be seen that alternate

Table 1
Number of lattice units (N) and downstream dependence analysis on time-averaged drag coefficient ($\overline{C}_D$) at $Re = 50$, $Da = 10^{-6}$.

Mesh size	N	$L_D = 25$		$L_D = 35$[a]		$L_D = 45$	
		$\overline{C}_D$	% Deviation	$\overline{C}_D$	% Deviation	$\overline{C}_D$	% Deviation
1380 × 900	30	1.934	15.235	1.896	16.145	1.895	16.102
1564 × 1020	34	1.862	10.963	1.702	4.307	1.702	4.295
1748 × 1140	38	1.746	4.004	1.658	1.575	1.657	1.538
1932 × 1260	42*	1.678	0.000	1.632	0.006	1.632	0.006
2116 × 1380	46	1.678	0.000	1.632	0.006	1.632	0.000
2300 × 1500	50	1.678	–	1.632	–	1.632	–

Table 2
Number of lattice units (N) and downstream dependence analysis on time-averaged mean Nusselt number ($\overline{Nu}_M$) at $Re = 50$, $Da = 10^{-6}$.

Mesh size	N	$L_D = 25$		$L_D = 35$[a]		$L_D = 45$	
		$\overline{Nu}_M$	% Deviation	$\overline{Nu}_M$	% Deviation	$\overline{Nu}_M$	% Deviation
1380 × 900	30	3.381	3.037	3.411	3.361	3.411	3.363
1564 × 1020	34	3.420	1.921	3.473	1.592	3.473	1.592
1748 × 1140	38	3.462	0.708	3.515	0.414	3.515	0.417
1932 × 1260	42[a]	3.487	0.003	3.529	0.000	3.529	0.003
2116 × 1380	46	3.488	0.029	3.529	0.000	3.529	0.000
2300 × 1500	50	3.487	–	3.529	–	3.529	–

[a] Number of lattices placed on characteristic length of the cylinder in this study.

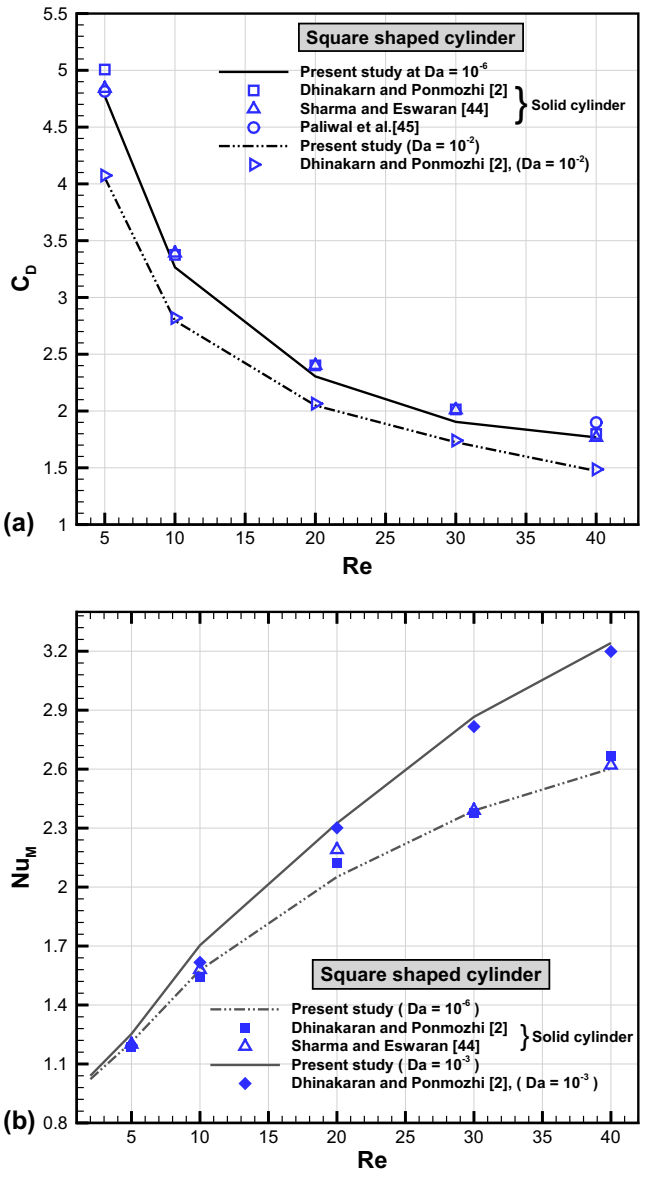

Fig. 2. Comparison of present simulation (square porous cylinder) results with literatures for $Pr = 0.71$. (a) Drag coefficient, C_D and (b) Mean Nusselt number, (Nu_M) for different values of Da.

negative (dotted line) and positive (solid line) vortices are being shed from front top and bottom slant surfaces of the cylinder, respectively for $Da \leqslant 10^{-3}$. At $Da = 10^{-6}$, the intensity of vortex shedding is significant and so, the size of vortices can be found to be large as well as far away from the symmetry line of the cylinder. It decays slowly with further increment of Da value. To impart further information on flow characteristics, the time-averaged vorticity contours are shown in Fig. 4(b) for different Da and at $Re = 150$. At a low permeability level (i.e. $Da = 10^{-6}$), the shear stress acting on the cylinder surface is higher than the other permeability levels. Consequently, the fluid particles start rotating on the cylinder surface and this intensity of rotation is transferred to external flow field. While enhancing the permeability, the velocity gradient around porous zone decreases which indicates the depletion of hydrodynamic boundary layer and this phenomenon is prominent at frontal edges of the cylinder. As a result, higher amount of fluid diffuses into the permeable cylinder and it can be seen in successive frames of Fig. 4(a) and (b). For all values of Re, the flow diffusion is observed to be more at $Da = 10^{-2}$. It is noticed that, while enhancing momentum of the fluid, time-averaged vorticity contours shift away from the symmetry line, indicating higher intensity of flow oscillation and vortex shedding. In the case of permeable cylinder, vortices are seen to move towards the symmetry line and this shows its ability on vortex shedding suppression. The diffused fluid in the porous cylinder losses its momentum due to relatively higher viscous forces offered by the porous zone, and thus, the intensity of vortex shedding diminishes. Therefore, it can be concluded that, vorticity strength is high at lower permeability values and due to vortex diffusion into the cylinder, strength of the same is found to be less in the case of higher permeable cylinder.

4.1.3. Time-averaged drag coefficient ($\overline{C}_D$) and pressure coefficient ($\overline{C}_p$)

The time-averaged drag coefficient experienced by the permeable diamond cylinder is evaluated from the momentum exchange method, and is presented in Fig. 5 for $50 \leqslant Re \leqslant 150$ for various values of Da. The drag coefficient of impermeable square cylinder with incident angle 45° is presented by Yoon et al. [14] and the same has been considered for comparison purpose. It can be seen that the variation of time-averaged drag coefficient ($\overline{C}_D$) with the increment of Re produces a small positive slope. From Fig. 5, we observe that at $Da = 10^{-6}$, the time-averaged drag coefficient values almost match with those of the solid cylinder case. The pressure difference between front and rear surfaces reduces due to the reduction of fluid obstruction offered by the cylinder at higher values of Da. On this account, irrespective of Re, the drag forces offered by the fluid decreases with an increase of Da. For example, at $Re = 60$, the time-averaged drag coefficients are found to be 1.641, 1.562, 1.34 and 0.8985 for non-dimensional permeability values of $10^{-6}, 10^{-4}, 10^{-3}$ and 10^{-2}, respectively. The drag value variation is observed to be different at $Da = 10^{-3}$ and 10^{-2}. At these values of Da, the time-averaged drag values reduce with the increase of Re. Thus, two different trends in the variation of time-averaged drag coefficient ($\overline{C}_D$) are reported. The variation of time-averaged pressure coefficient ($\overline{C}_p$) on the surface of the porous diamond-shaped cylinder is shown in Fig. 6 for different values

Table 3
Comparison of calculated time-averaged drag coefficient ($\overline{C}_D$) for different *Re* and *Pr* = 0.71 with Yoon et al. [14] for the case of a solid diamond-shaped cylinder in an unbounded flow domain for $40 \leqslant Re \leqslant 100$.

S.No.	*Re*	Time-averaged drag coefficient ($\overline{C}_D$)		
		Present study	Yoon et al. [14]	% Deviation
1	40	1.58452	1.57868	0.369
2	50	1.60313	1.58711	1.000
3	60	1.63212	1.61912	0.796
4	70	1.66607	1.64630	1.186
5	80	1.69622	1.67678	1.146
6	90	1.73739	1.71096	1.521
7	100	1.75445	1.74116	0.758

Table 4
Comparison of calculated mean Nusselt number (Nu_M) for $Da = 10^{-6}$ and 10^{-3} at *Pr* = 0.71 with Rashidi et al. [21] for the case of permeable diamond-shaped cylinder in an unbounded flow domain for $5 \leqslant Re \leqslant 40$.

S.No.	*Re*	$Da = 10^{-6}$			$Da = 10^{-3}$		
		Present study	Rashidi et al. [21]	% Deviation	Present study	Rashidi et al. [21]	% Deviation
1	5	1.49696	1.49038	0.439	1.53947	1.53846	0.066
2	10	1.91962	1.85577	3.326	1.99951	1.98077	0.938
3	20	2.49371	2.47115	0.904	2.66340	2.65385	0.359
4	30	2.92318	2.91346	0.332	3.18184	3.16346	0.578
5	40	3.28956	3.25962	0.910	3.63125	3.59615	0.967

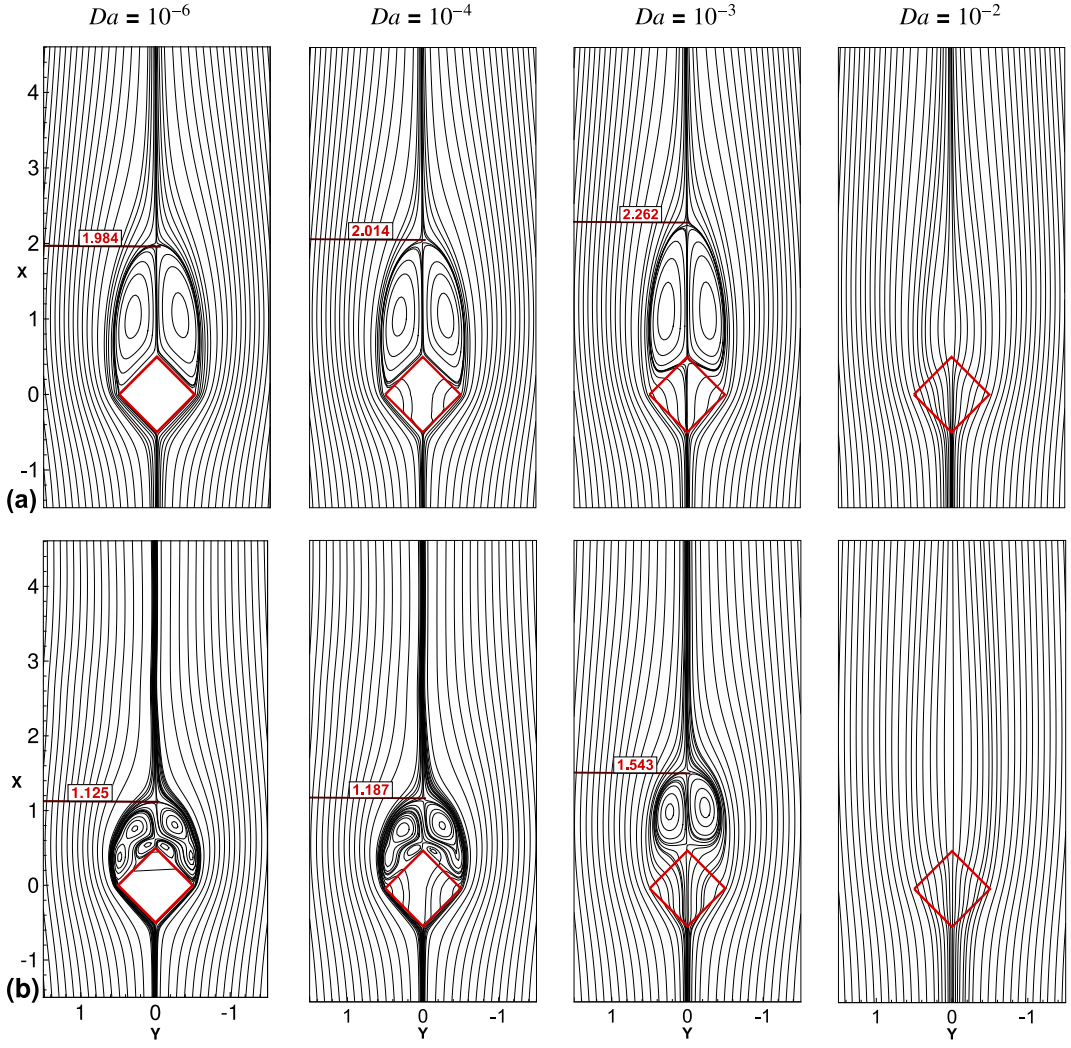

Fig. 3. Streamlines of time-averaged mean flow around and through permeable diamond-shaped cylinder at (a) *Re* = 50 and (b) *Re* = 150 for various *Da*.

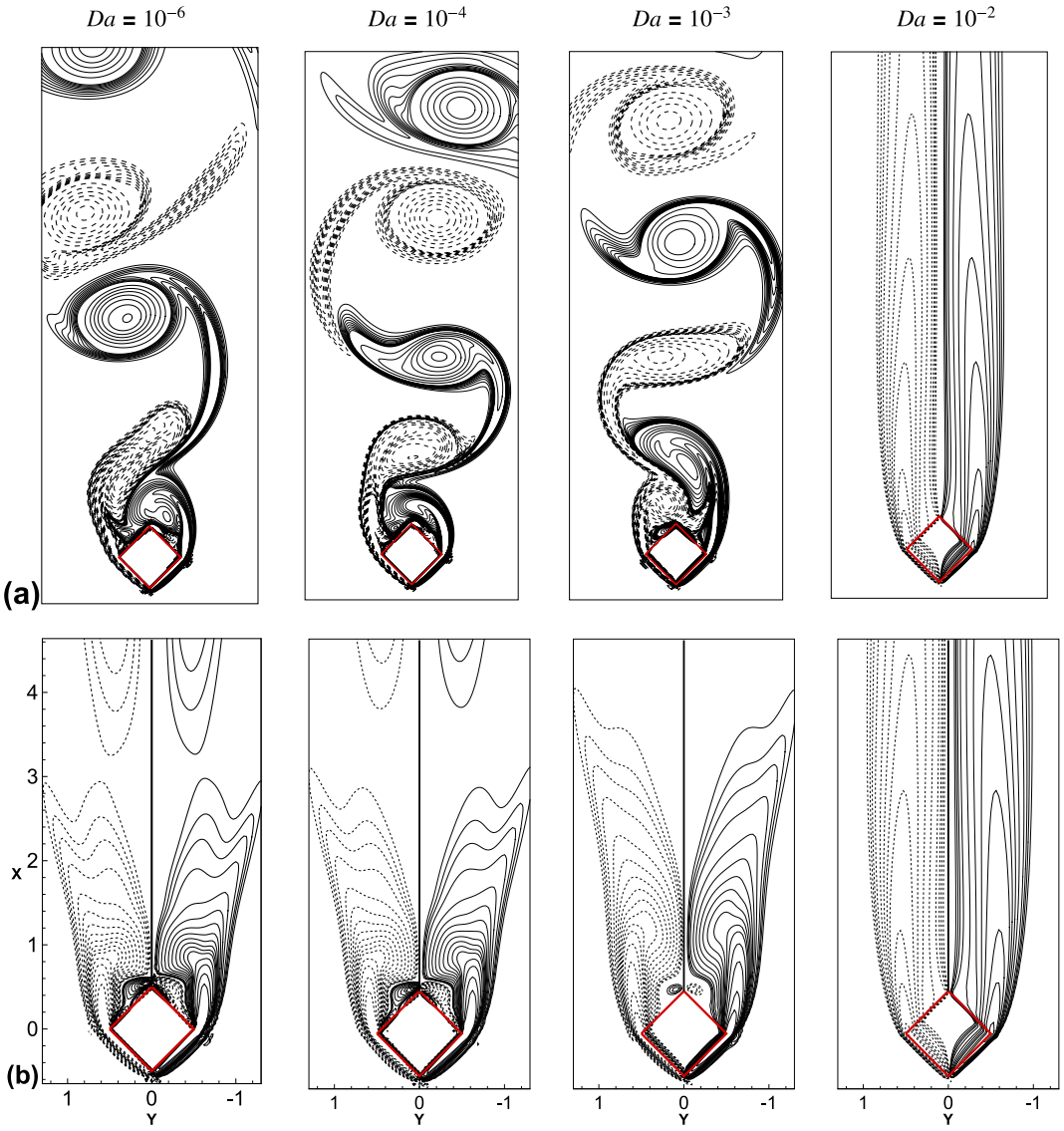

Fig. 4. (a) Instantaneous and (b) time-averaged vorticity contours of flow around and through a permeable diamond-shaped cylinder at $Re = 150$ for various Da.

of Darcy number at $Re = 150$. It is seen that for all values of Reynolds number, the pressure stagnates at the centre point of frontal surface (corner A) and it gradually reduces as the fluid moves over the surface. Further, it reaches to a minimum value of pressure at corner B and D. At rear surface of the cylinder, the momentum of the fluid is relatively lesser than that of frontal area and hence, the value of $\overline{C}_p$ gradually increases up to the corner C. The same phenomenon has been addressed by Yoon et al. [14] in their study. The increment of Da for a constant value of Re, produces the monotonous pressure reduction and increment at front and rear surfaces, respectively and such variations are notable while increasing the value of Re. This is evident for the reduction of time-averaged drag coefficient with the increment of Da. As the fluid completely enters into the body at $Da = 10^{-2}$, the pressure value reduction at front surfaces is very less in comparison to other values of Darcy number. It should be noted that the pressure difference between corner A and C indicates the pressure drop across the cylinder. From Fig. 6, one can see the pressure drop reduction across the cylinder due to the increment of Da.

4.1.4. Variation of time-averaged wake saddle point

Non-dimensional permeability (Da) impacts the flow pattern, inturn causing the movement of saddle point (i.e. reattachment point) of recirculation region. Fig. 7 shows the variation of wake saddle point (time-averaged) from the center of cylinder (L_r) as a function of Re and Da. In the case of steady flow, reattachment point of the wake shifts away from the cylinder with Re due to inertial force dominance. But this trend becomes completely reversed in the case of unsteady flow. The wake saddle point approaches the cylinder with the increasing Re for all values of Da. Rich permeable cylinder allows more fluid into it. As a result of this, the separation point moves forward from top/bottom corner of the cylinder downstream, the wake reattachment point also moves forward. Therefore, wake saddle point moves away from the cylinder with the increase of Da for a constant value of Re. Also, for $10^{-6} \leqslant Da \leqslant 10^{-4}$, this L_r increment is observed to be monotonous and it is substantial at $Da = 10^{-3}$. However, from Fig. 3, it is evident that higher permeability values can also reduce the size of recirculation zone in both x and y-directions. This also implies that the

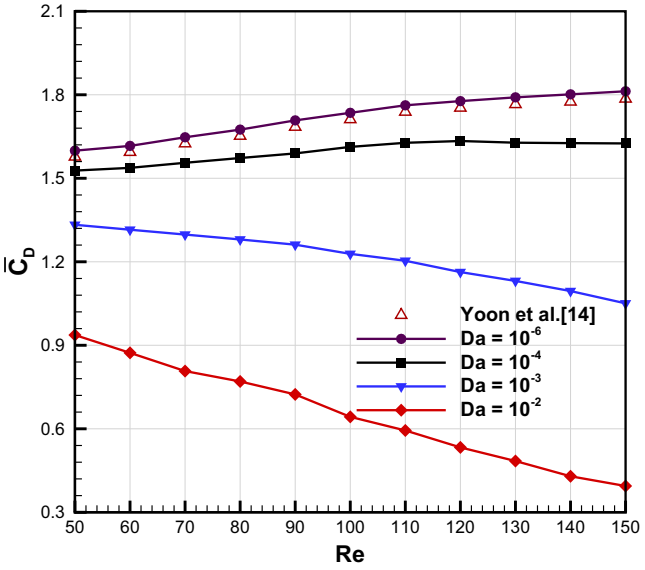

Fig. 5. Variation of time-averaged drag coefficient ($\overline{C}_D$) at various Reynolds number ($50 \leqslant Re \leq 150$) for $Da = 10^{-6}, 10^{-4}, 10^{-3}$ and 10^{-2}.

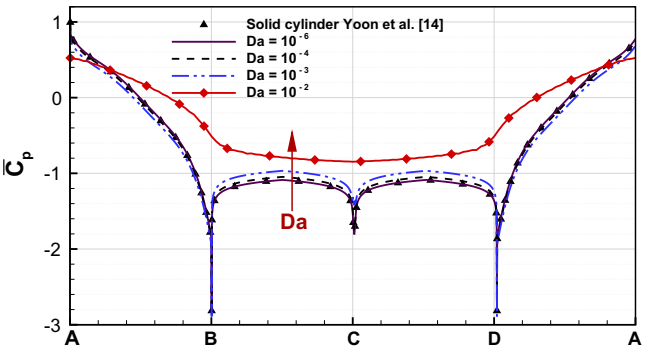

Fig. 6. Distribution of time-averaged pressure coefficient ($\overline{C}_p$) on the surface of the porous diamond-shaped cylinder at $Re = 150$ for different values of Da.

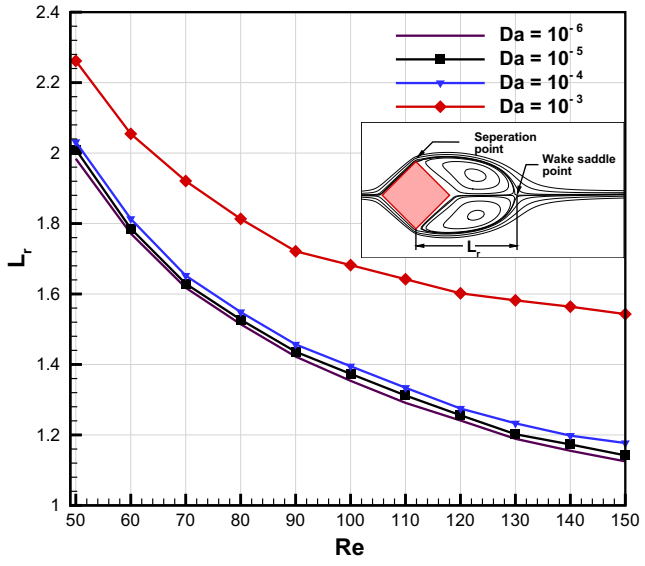

Fig. 7. Variation of time-averaged recirculation length (L_r) with Reynolds and Darcy numbers for flow over a permeable diamond-shaped shaped cylinder.

intensity of vortex shedding can be greatly altered with higher permeability values. At $Da = 10^{-2}$, almost all fluid passes through the cylinder, suppressing vortex shedding and wake at the downstream of permeable cylinder.

4.1.5. Time evolution of lift coefficient

In order to show the effect of permeability on vortex shedding, the lift coefficients were calculated at each time instants and presented in Fig. 8(a) and (b) at start of vortex flow and dynamic steady state, respectively, for different values of Da at $Re = 100$. In the unsteady case, along with drag force, the lift force (i.e. force in y-direction) also acts on the cylinder and it oscillates with respect to time. The mean lift value of cylinder with 0°&45° incident angle is zero [14] and the same can be seen for different Da values. It is seen that the amplitude of lift coefficient increases with the increment in Re irrespective of non-dimensional permeability. The lift oscillations occur for $Da = 10^{-3}$ later than $Da = 10^{-4}$ and 10^{-6} with less amplitude. This implies that the vortex shedding appearance can be delayed by increasing Da value. For $Da = 10^{-6}$, the vortex shedding starts early with respect to time followed by 10^{-4} and 10^{-3}. In addition, the amplitude of oscillation is observed to be greater under lower permeable condition with relatively lower frequency of oscillation. A finite amount of fluid which enters into permeable cylinder reduces the resultant shear and pressure forces acting in the y-direction. Hence, the amplitude of lift force oscillation is less for the case permeable cylinders. The same scenario has been observed for all other Re and Da ranges considered in this study. This shows the influence of porous diamond-shaped body on the reduction of lift force amplitude. It should be noted that in the case of square cylinder, while increasing Da, the amplitude of lift force also increases. Hence, to avoid flow instabilities, the square permeable body needs to be oriented to 45° (diamond-shape) with reference to flow direction. Also, $Da = 10^{-2}$, the lift coefficient becomes zero for the ranges of Re considered in present study.

4.1.6. Vortex suppression

It is well known from the flow characteristics that, fluid flows through the cylinder completely without formation of wake or vortex structures downstream at $Da = 10^{-2}$ for all values of Re. On the other hand, it is quite difficult to obtain a non-dimensional permeability up to 10^{-2} experimentally [46]. Thus it is important to understand the flow phenomenon between 10^{-3} and 10^{-2}. Fig. 9 shows ranges of Da values, where vortex suppression and wake formation and suppression occurs for different values of Re. The vortices that form behind the cylinder at lower Re, requires less increment in permeability to suppress it. Whereas, in case of higher Re, the same suppression can be achieved only at higher values of Da. Upon increasing permeability levels, asymmetric wake formation occurs followed by detached symmetric wake behind the cylinder. It is seen that the wake detachment from cylinder forms at higher values of Da in the case of lower Re. Due to the enhancement in fluid momentum, same phenomenon happens at lower permeability range and it can be seen in Fig. 9 at higher Re values. Therefore, the range of non-dimensional permeability for wake suppression is more at low Re and it decreases with an increase of Re. Furthermore, the detached wake moves forward and also it suppresses due to the reduction of fluid restriction. The Da values required for the wake depletion decays with the increment of Re. Hence, higher velocity fluids need large permeability values to suppress vortex shedding and the same needs to be less to suppress wake.

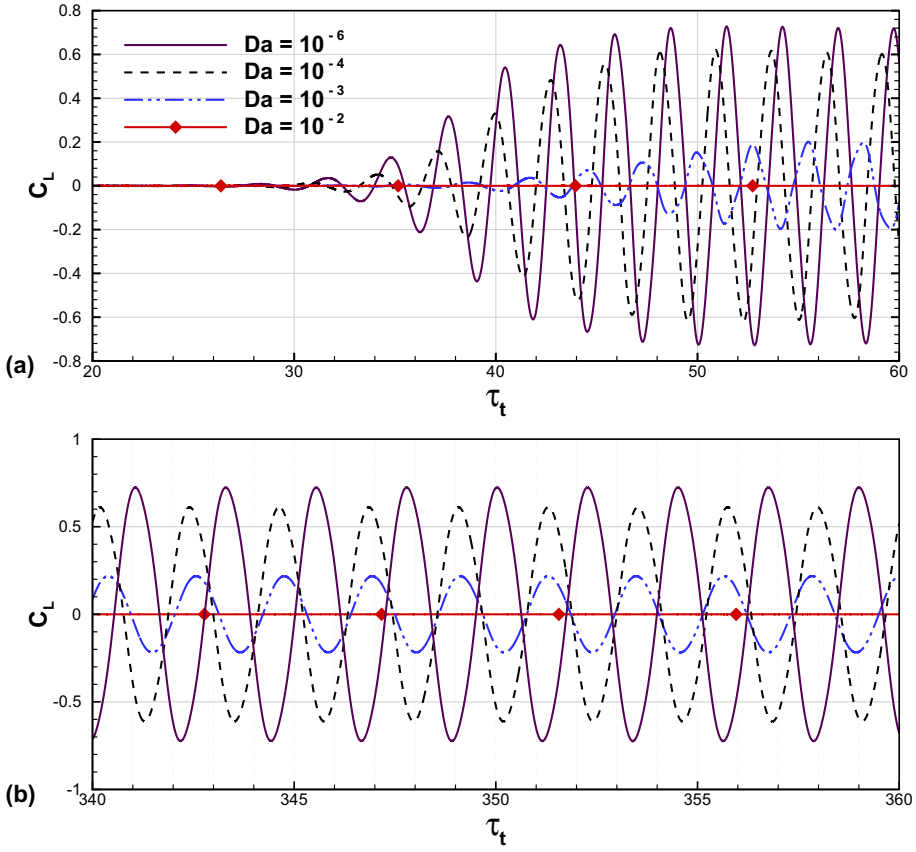

Fig. 8. Time evolution of lift coefficient (C_L) at (a) start of vortex flow and (b) dynamic steady state for various Darcy number and at *Re* = 100 for flow around and through a diamond-shaped porous cylinder. Legend in (a) is also applicable to (b).

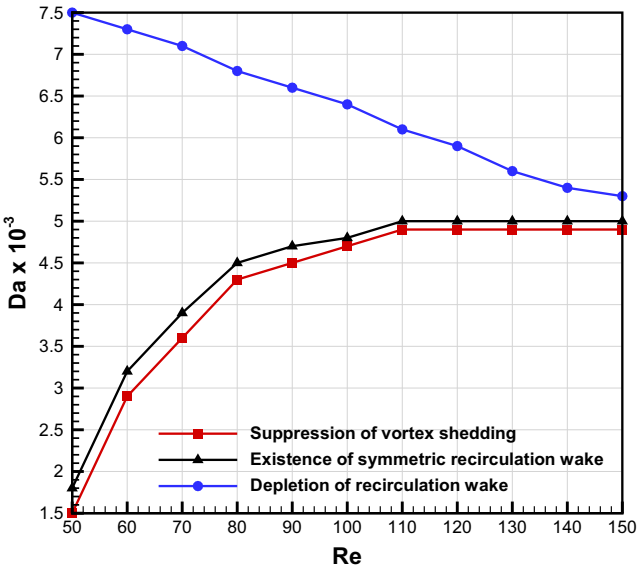

Fig. 9. Effect of Darcy number on vortex and wake suppression at various Reynolds number ($50 \leqslant Re \leq 150$) for flow through and around a permeable diamond-shaped cylinder.

4.2. Heat transfer characteristics

4.2.1. Isotherms

As the flow considered in this study is in laminar unsteady flow regime, it is noticed that two rows of warm blobs being convected from the cylinder to its downstream. Also, it is observed that a wavering motion at the downstream of the cylinder exists. The thermal field continually grows on front slant surfaces of cylinder and it eventually breaks off from the top and bottom corner of it. The temperature distribution around the cylinder is affected by fluid momentum and non-dimensional permeability. The clear behaviour of thermal field can be obtained from time-averaged isotherms, where we can observe the thermal cloud variation. The influence of *Da* variation on heat transfer characteristics of a permeable diamond-shaped cylinder in unsteady regime is presented through time-averaged isotherms around the cylinder in Fig. 10(a) and (b). At *Re* = 50 and $Da = 10^{-6}$, a thumb like projection of isotherms can be seen at downstream of the cylinder. The curvature of this thumb projection moves towards rear faces of the cylinder with the increase of *Re*. Thermal clustering on front faces of the cylinder is evident for maximum heat transfer and the reduction of thermal boundary layer at these surfaces relative to rear surfaces. With an increase of permeability, one can notice the increase of thermal plume at downstream of the cylinder. As a higher permeable cylinder allows more fluid flow through in it, the temperature gradient becomes large which also results in reduction of thermal boundary layer thickness. However, this layer thickness increases while increasing permeability value at rear surfaces of the cylinder. This is due to the reason that the penetrated fluid carries away more heat from the front slant surfaces. Furthermore, the time-averaged isotherm patterns along with the velocity vector variation for *Re* = 100 is depicted in Fig. 11 for different *Da* values. It is to be noted that in Fig. 11, if the vector line is long, the magnitude of velocity at that point is high. For all values of *Da*, the velocity vectors are seen to be crowded with greater magnitude

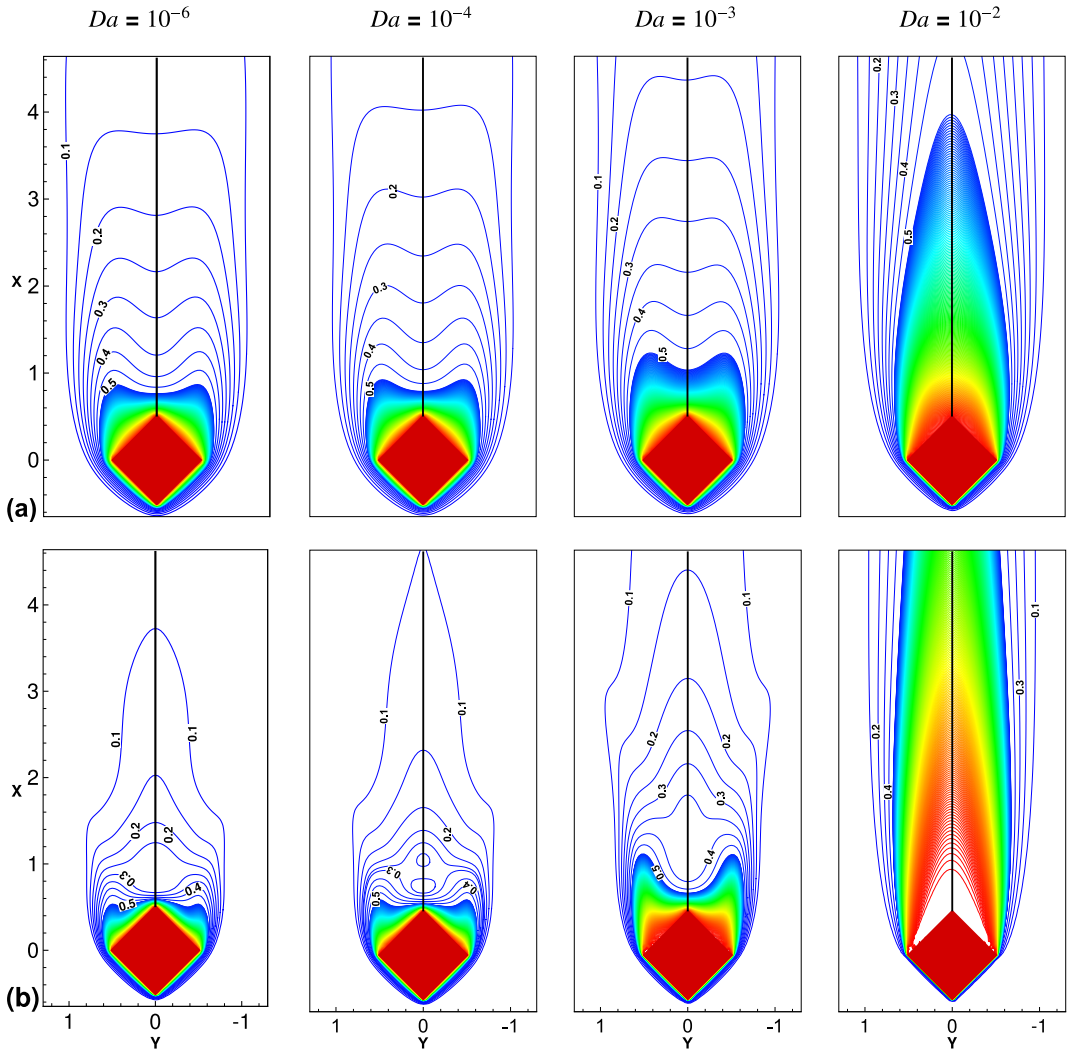

Fig. 10. Time-averaged isotherm contours of mean flow around and through a permeable diamond-shaped cylinder at (a) Re = 50 and (b) Re = 150 for various Da.

at front face of the cylinder, which is the reason for higher heat transfer rate at this surface. With careful observation, one can see that the magnitude of velocity in the porous zone increases with Darcy number and hence, the thermal plume at rear surface sparsely distributed. For instance, one can see the position variation of isotherm contour 0.9 for different values of Da. Also, at rear face of the cylinder, the magnitude of velocity is found to be more while enhancing the permeability. Due to the restriction of fluid flow at lower permeability values, the isotherm pattern is not as much narrower as at $Da = 10^{-2}$. This implies that relatively very low heat is convected from the cylinder and that the rate of convection increases with the increase of Da.

4.2.2. Heat transfer enhancement along the cylinder surface

To bring out the effect of Da on heat transfer rate at each surface of the cylinder, the heat transfer enhancement ratio (E) is calculated from Eq. (29) for all the surfaces of cylinder, and is presented in Fig. 12. Firstly, the time-averaged Nusselt number at each surface is evaluated through local time-averaged Nusselt number and then the enhancement ratio is calculated with reference to $\overline{Nu}$ at $Da = 10^{-6}$. Fig. 12(a) shows the enhancement of heat transfer rate with the increase in Da values. The enchantment ratio at these surfaces increases with an increase of fluid momentum for all Da values. Due to the direct contact of fluid on frontal surfaces of cylinder, the thermal boundary layer becomes thin and hence, the E_{AB}&E_{AD} increases with Re. The depletion rate of thermal boundary layer becomes more while allowing more fluid in the porous zone. Thus, heat transfer enhancement can be noticed while increasing non-dimensional permeability values. This enhancement is found to be very less at $Da = 10^{-4}$ and the same is observed to be substantial at $Da = 10^{-3}$. However, an extensive heat enhancement rate occurs at $Da = 10^{-2}$ due to large fluid penetration. For instance, the E_{AB} or E_{AD} of permeable diamond cylinder at Re = 80 at $Da = 10^{-2}$ is 2.492, whereas it has a value of 1.077 and 1.407 at $Da = 10^{-4}$ and 10^{-3}, respectively. Fig. 10 indicates sparse distribution of isotherms at rear surfaces of the cylinder and the gap between isotherms increase with an increase of Darcy number. This implies that the thermal boundary layer thickness increases at these surfaces while cylinder turns to be more permeable. As a result of this, heat transfer detraction occurs while increasing permeability value and it is prominent at higher values of Re. Fig. 12 (b) elucidates the same behaviour on heat transfer enhancement ratio at rear faces of the cylinder. At $Da = 10^{-2}$, a large amount of fluid enters into the cylinder and as a result of this, the temperature gradient at faces BC and CD reduces drastically. Hence, at all Re, the heat transfer reduction is observed for the case of $Da = 10^{-2}$ with reference to 10^{-6}. However, as like frontal surface variation on heat transfer, at $Da = 10^{-4}$ the rear faces also have very less variation on E.

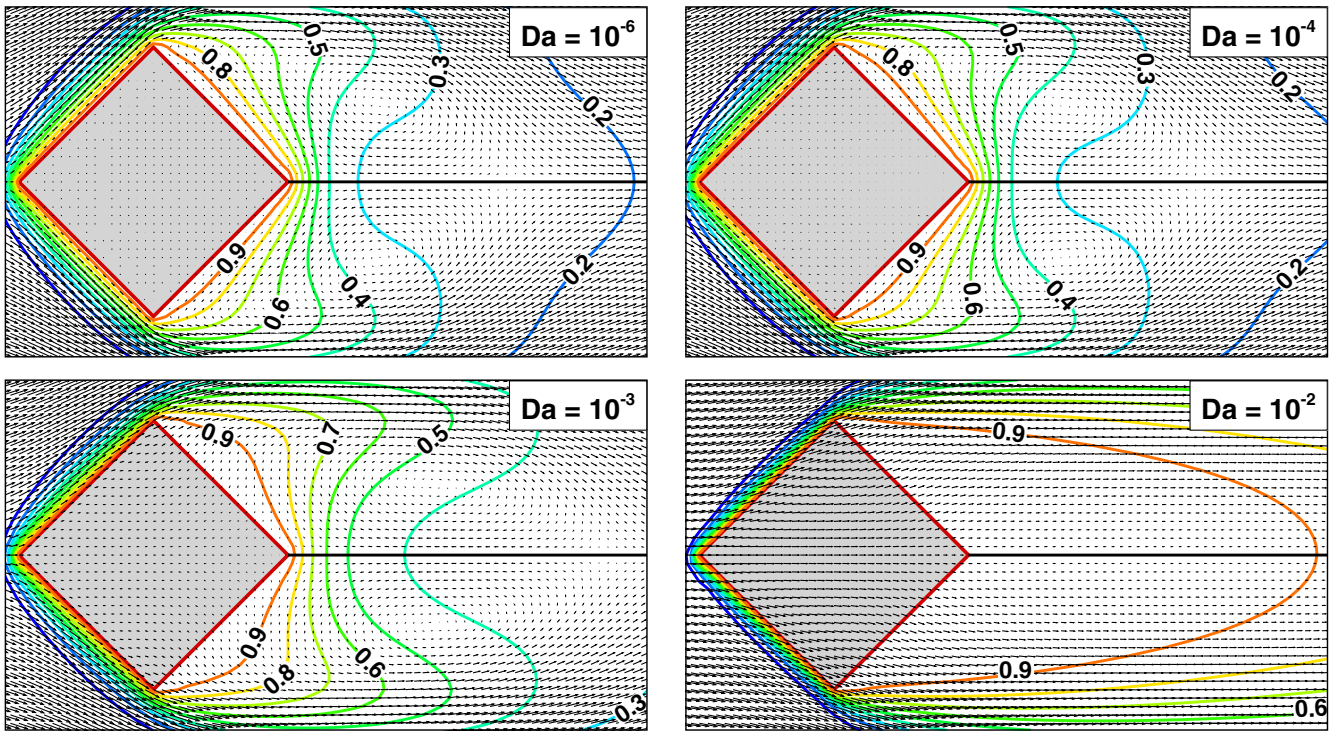

Fig. 11. Time-averaged vector and isotherm plots of mean flow around and through a permeable diamond-shaped cylinder at $Re = 100$ for different values of Da.

4.2.3. Average mean Nusselt number ($\overline{Nu}_M$)

Permeability effects on overall heat transfer rates can be quantified by comparing time-averaged mean Nusselt number at different values of Re and Da. The variation of $\overline{Nu}_M$ at various permeability levels and $50 \leqslant Re \leqslant 150$ have been presented in Fig. 13(a) for flow across and through diamond-shaped permeable cylinder. The linear increment on time-averaged mean Nusselt number depicts that the heat transfer rate is a function of Re. As discussed earlier in Sections 4.2.1 and 4.2.2, due to the decrement of thermal boundary layer and large thermal gradient at higher fluid velocity, heat dissipation increases with increasing Re. Although, a different trend of heat enhancement ratio is observed on front and rear surfaces of the cylinder, the overall thermal characteristics enhances with the increment of Da. The average mean Nusselt number variation between $Da = 10^{-6}\&10^{-4}$ is found to be less. Whereas, for $Da > 10^{-4}$ the enhancement can be seen to be more prominent. At $Da = 10^{-4}$, due to large deviation in fluid path and less fluid velocity in porous region, the heat transfer rate is less significant than other higher values of non-dimensional permeability values. The low values of temperature gradient on frontal surfaces of the cylinder at rich permeable values (i.e. $Da = 10^{-2}$), dominates over low heat dissipation rate of rear surfaces. As a result of this, the heat transfer enrichment is drastic for this permeability range. In addition, the permeability variation on heat transfer augmentation is more at higher values of Re. For instance, the enhancement ratios of $\overline{Nu}_M$ at $Re = 50$ for $Da = 10^{-4}, 10^{-3}\&10^{-2}$ are 1.02, 1.13 and 1.69, respectively. Whereas, for the same Da values at $Re = 100$ the ratio is 1.04, 1.24 and 2.

Non-linear regression method is used to build correlation between time-averaged Nusselt number, Reynolds number and non-dimensional permeability. It is found that the time-averaged mean Nusselt number is a function of $Re^{0.572}$ and $Da^{0.095}$, and the proportionality fits present data satisfactorily.

In order to compare the heat transfer variation of square and diamond-shaped permeable cylinders at different Darcy numbers, a comparative study on the variation of time-averaged mean Nusselt number of these cylinders is carried out at $Re = 50$, 100 and 150 for different values of Da and it is presented in Fig. 13(b). In the case of square cylinder, only one face of the cylinder is in direct contact with the flow. If the same square cylinder is tilted to an angle of 45° (i.e. diamond-shaped cylinder), two front surfaces directly contact the incoming fluid and hence, thermal boundary layer reduction occurs at these surfaces. Therefore, in comparison to the square cylinder, diamond-shaped cylinder shows enhanced heat transfer characteristics at frontal area for all values of Re and Da. In addition, it is evident that at higher Da, the frontal surface dissipates more heat than any other surface. At rear side, square cylinder has only one surface whereas, diamond-shaped cylinder has two. At this surface, the boundary layer thickness is more and it increases with the increase in permeability level. Accordingly, the heat transfer rate at rear surface of diamond cylinder decays at rich Da condition. Although only one rear surface exists in square cylinder, the cumulative effect on heat transfer is lesser than diamond-shaped cylinder, as shown in Fig. 13(b). The percentage increase in average mean Nusselt number of permeable diamond cylinder decreases monotonously with the increase of non-dimensional permeability up to 10^{-3}. For an instance, for $Re = 100$ the percentage enhancement of diamond-shaped cylinder at $Da = 10^{-6}, 10^{-4}, 10^{-3}$ and 10^{-2} is 15.87%, 15.37%, 12.95% and 21.84%, respectively with reference to permeable square cylinder. This is due to the dominance of two rear thermal boundary layers on heat transfer. However, at $Da = 10^{-2}$, the influence of frontal surfaces is more than the rear and thus, at this condition the percentage enhancement of diamond shaped cylinder is high.

5. Conclusions

The flow and heat transfer characteristics of a permeable diamond-shaped cylinder, placed in a uniform flow and maintained at a constant temperature, are studied in detail using the D2Q9 lattice model of LBM. The Darcy-Forchheimer force term,

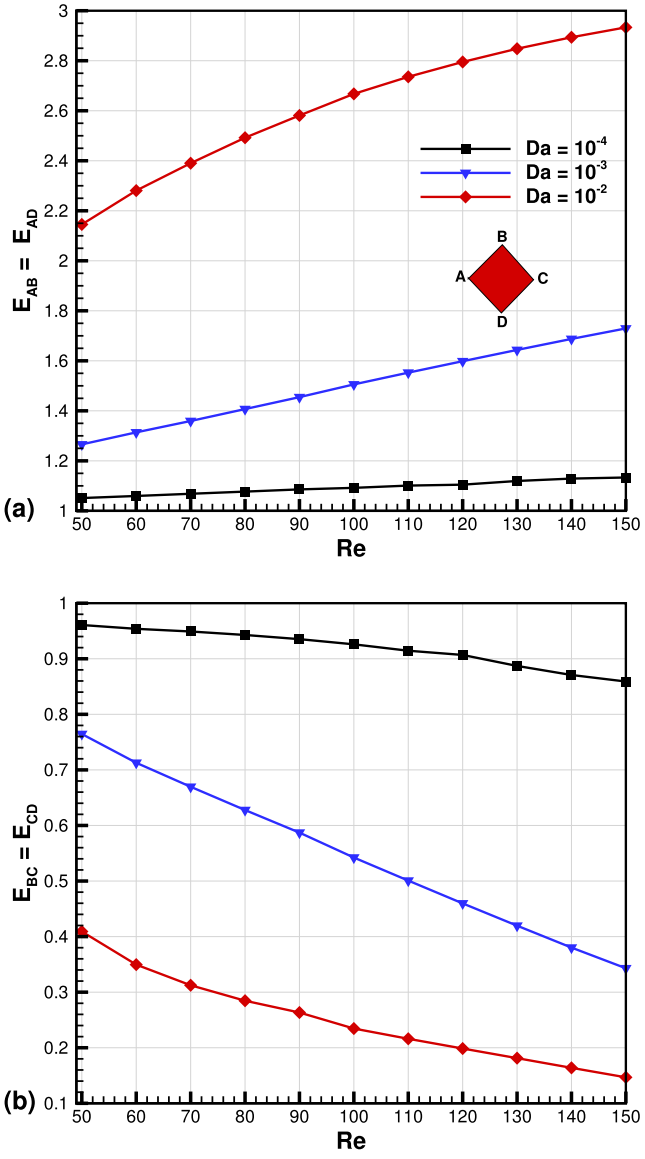

Fig. 12. Effect of Darcy number on heat transfer enhancement ratio at different Reynolds number on (a) front top (AB)/bottom (AD) face and (b) rear top (BC)/bottom (CD) face of the heated permeable diamond-shaped cylinder in an unbounded domain. Legend in (a) is also applicable to (b).

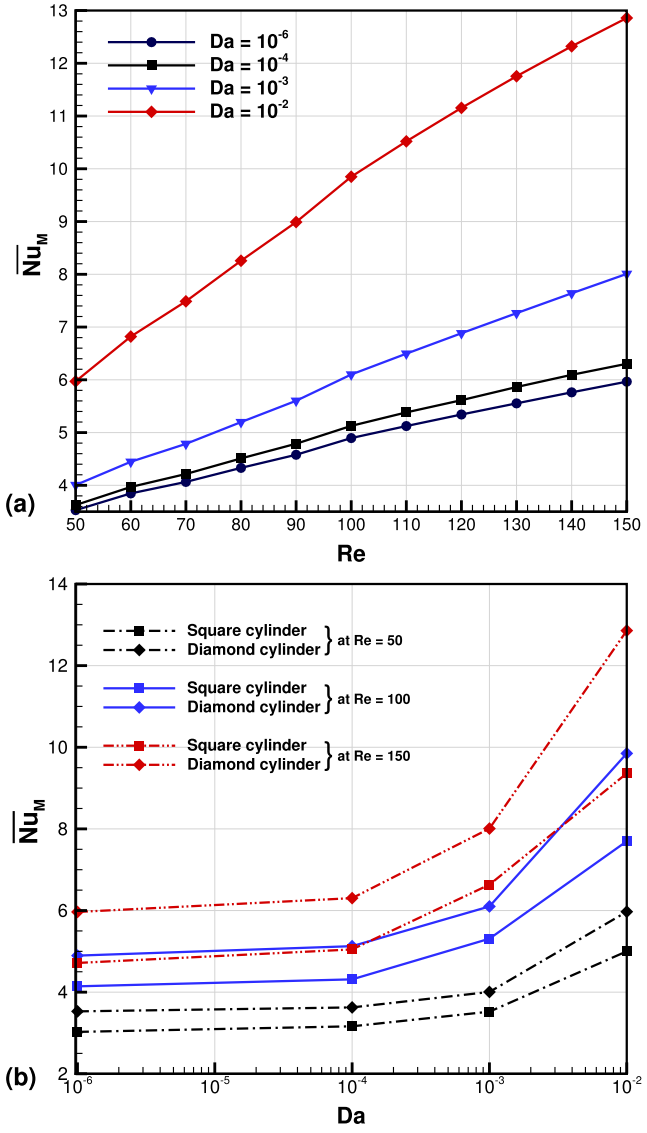

Fig. 13. (a) Effect of Darcy number on time-averaged mean Nusselt number ($\overline{Nu}_M$) at different values of Reynolds number ($50 \leqslant Re \leqslant 150$) for flow around and through a permeable diamond-shaped cylinder; (b) Time-averaged mean Nusselt number ($\overline{Nu}_M$) comparison between permeable square and diamond-shaped cylinder at Re = 50, 100 and 150 for different values of Da.

which has the viscous and form drag terms of porous medium, is added to the SRT-BGK collision equation. The effects of permeability on flow and thermal configuration have been studied for: Re = 50–100, $Da = 10^{-6} - 10^{-2}$ and Pr = 0.71. The important results can be summarized as follows:

- With the increase of permeability from the solid cylinder limit ($Da > 10^{-6}$), gradually more fluid flows through the cylinder due to the reduction of viscous drag term inside the cylinder. Due to this reason, reduction of vortex shedding strength is observed and further it completely vanishes at $Da = 10^{-2}$ for all Re considered in this study. As a result of reduction in hydrodynamic boundary layer at higher Da, the vortex diffusion into the cylinder is found to be more.
- The time evolution of lift forces show that the intermediate permeable cylinder could delay the vortex phenomenon compared to the impermeable case. A finite amount of fluid penetration reduces the pressure and viscous forces on the cylinder which results in reduction of the drag coefficient for same value of Re. Higher permeable cylinder changes the separation point of fluid and hence, the stagnation point of wake moves ahead from the rear surface. Permeability level required to suppress the vortex phenomenon is directly proportional to Re, whereas, it is inversely proportional in case of wake suppression.
- Thermal gradient at the front portion of the cylinder gradually increases with the increase in Darcy number and Reynolds number. Relatively, the thermal boundary layer thickness is observed to be more on rear slant edges of the cylinder with the increase of permeability. However, the net heat transfer rate progressively increases with Da at constant Re.
- Thick and narrow thermal plume at higher Da, suggests heat transfer augmentation, while at $Da = 10^{-2}$ it is reported to be maximum for all values of Re. The average mean Nusselt number value of diamond-shaped cylinder is found to be higher than that of a square-shaped cylinder at different permeability levels due to the influence of frontal surface thermal boundary layer.

- Finally, to quantify the time-averaged mean Nusselt number at different Darcy numbers, a correlation as a function of *Re* and *Da* is obtained, which shows the dominance of *Re* and *Da* on heat transfer performance.

Thus, we can conclude that the choice of Darcy number and the shape of the porous bluff body are crucial while modeling a porous medium for real-time heat transfer applications.

Future work

Thermal boundary layer formation on porous body can be greatly altered by varying the incident angle of flow. Furthermore, the real-time heat dissipation systems such as porous heat sink, pin-fin apparatus and LED backlight module etc., are significantly influenced by the viscous layers of top and bottom wall along with different thermal boundary conditions. Hence, a detailed numerical analysis can be carried out at different incident angles of flow on porous square zone with the effect of channel confinement to identify the maximum heat dissipation condition.

Conflict of interest

Authors declare that there is no conflict of interest.

Acknowledgement

One of the authors, S. Dhinakaran, gratefully acknowledges the fund received from Council of Scientific & Industrial Research (CSIR), Government of India, through a project grant (Project Reference No. 22(0642)/13/EMR-II) for carrying out this work.

References

[1] S. Bhattacharyya, S. Dhinakaran, A. Khalili, Fluid motion around and through a porous cylinder, Chem. Eng. Sci. 61 (13) (2006) 4451–4461.
[2] S. Dhinakaran, J. Ponmozhi, Heat transfer from a permeable square cylinder to a flowing fluid, Energy Convers. Manage. 52 (5) (2011) 2170–2182.
[3] M.R. Khorrami, M.M. Choudhari, Application of Passive Porous Treatment to Slat Trailing Edge Noise, Technical Report NASA/TM-2003-212416, NASA, 2003.
[4] P. Yu, T.S. Lee, Y. Zeng, H.T. Low, Fluid dynamics and oxygen transport in a micro-bioreactor with a tissue engineering scaffold, Int. J. Heat Mass Transf. 52 (1) (2009) 316–327.
[5] P. Yu, Y. Zeng, T.S. Lee, X.B. Chen, H.T. Low, Steady flow around and through a permeable circular cylinder, Comput. Fluids 42 (1) (2011) 1–12.
[6] D. Poulikakos, M. Kazmierczak, Forced convection in a duct partially filled with a porous material, J. Heat Transf. 109 (3) (1987) 653.
[7] S. Chikh, A. Boumedien, K. Bouhadef, G. Lauriat, Analytical solution of non-Darcian forced convection in an annular duct partially filled with a porous medium, Int. J. Heat Mass Transf. 38 (9) (1995) 1543–1551.
[8] H. Sung, Forced convection from an isolated heat source in a channel with porous medium, Fuel Energy Abstr. 37 (3) (1996) 232.
[9] P. Yu, Y. Zeng, T. Lee, H. Bai, H. Low, Wake structure for flow past and through a porous square cylinder, Int. J. Heat Fluid Flow 31 (2) (2010) 141–153.
[10] T.-C. Jue, Numerical analysis of vortex shedding behind a porous square cylinder, Int. J. Numer. Methods Heat Fluid Flow 14 (5) (2004) 649–663.
[11] X. Chen, P. Yu, S. Winoto, H.-T. Low, Numerical analysis for the flow past a porous square cylinder based on the stress-jump interfacial-conditions, Int. J. Numer. Methods Heat Fluid Flow 18 (5) (2008) 635–655.
[12] H.-W. Wu, R.-H. Wang, Convective heat transfer over a heated square porous cylinder in a channel, Int. J. Heat Mass Transf. 53 (9) (2010) 1927–1937.
[13] W.-S. Fu, H.-C. Huang, W.-Y. Liou, Thermal enhancement in laminar channel flow with a porous block, Int. J. Heat Mass Transf. 39 (10) (1996) 2165–2175.
[14] D.-H. Yoon, K.-S. Yang, C.-B. Choi, Flow past a square cylinder with an angle of incidence, Phys. Fluids 22 (4) (2010) 043603.
[15] S. Dutta, P. Panigrahi, K. Muralidhar, Effect of orientation on the wake of a square cylinder at low Reynolds numbers, Indian J. Eng. Mater. Sci. 11 (2004) 447–459.
[16] S. Miran, C.H. Sohn, Influence of incidence angle on the aerodynamic characteristics of square cylinders with rounded corners: a numerical investigation, Int. J. Numer. Methods Heat Fluid Flow 26 (1) (2016) 269–283.
[17] S.R. Djeddi, A. Masoudi, P. Ghadimi, Numerical simulation of flow around diamond-shaped obstacles at low to moderate Reynolds numbers, Am. J. Appl. Math. Stat. 1 (1) (2013) 11–20.
[18] W. Regulski, J. Szumbarski, Numerical simulation of confined flows past obstacles–the comparative study of lattice Boltzmann and spectral element methods, Arch. Mech. 64 (4) (2012) 423–456.
[19] M.S. Valipour, S. Rashidi, M. Bovand, R. Masoodi, Numerical modeling of flow around and through a porous cylinder with diamond cross section, Eur. J. Mech.-B/Fluids 46 (2014) 74–81.
[20] S. Rashidi, R. Masoodi, M. Bovand, M. Sadegh Valipour, Numerical study of flow around and through a porous diamond cylinder in different apex angles, Int. J. Numer. Methods Heat Fluid Flow 24 (7) (2014) 1504–1518.
[21] S. Rashidi, M. Bovand, I. Pop, M. Valipour, Numerical simulation of forced convective heat transfer past a square diamond-shaped porous cylinder, Transp. Porous Media 102 (2) (2014) 207–225.
[22] A.A. Mohamad, Lattice Boltzmann Method: Fundamentals and Engineering Applications with Computer Codes, Springer Science & Business Media, 2011.
[23] R. Mohebbi, M. Nazari, M.H. Kayhani, Comparative study of forced convection of a power-law fluid in a channel with a built-in square cylinder, J. Appl. Mech. Tech. Phys. 57 (1) (2016) 55–68.
[24] R. Mei, L.-S. Luo, W. Shyy, An accurate curved boundary treatment in the lattice Boltzmann method, J. Comput. Phys. 155 (2) (1999) 307–330.
[25] J. Bao, P. Yuan, L. Schaefer, A mass conserving boundary condition for the lattice Boltzmann equation method, J. Comput. Phys. 227 (18) (2008) 8472–8487.
[26] M. Nazari, R. Mohebbi, M. Kayhani, Heat transfer enhancement in a channel partially filled with a porous block: lattice Boltzmann method, Int. J. Mod. Phys. C 24 (09) (2013) 1350060.
[27] M. Nazari, R. Mohebbi, M. Kayhani, Power-law fluid flow and heat transfer in a channel with a built-in porous square cylinder: lattice Boltzmann simulation, J. Nonnewton. Fluid Mech. 204 (2014) 38–49.
[28] Z. Guo, T. Zhao, Lattice Boltzmann model for incompressible flows through porous media, Phys. Rev. E 66 (3) (2002) 036304.
[29] Z. Guo, T. Zhao, A lattice Boltzmann model for convection heat transfer in porous media, Numerical Heat Transfer, Part B 47 (2) (2005) 157–177.
[30] V. Babu, A. Narasimhan, Investigation of vortex shedding behind a porous square cylinder using lattice Boltzmann method, Phys. Fluids 22 (5) (2010) 053605.
[31] T.R. Vijaybabu, K. Anirudh, S. Dhinakaran, Mixed convective heat transfer from a permeable square cylinder: a lattice Boltzmann analysis, Int. J. Heat Mass Transf. 115 (2017) 854–870.
[32] S. Chen, D. Martinez, R. Mei, On boundary conditions in lattice Boltzmann methods, Phys. Fluids 8 (9) (1996) 2527–2536.
[33] Q. Liu, Y.-L. He, Q. Li, W.-Q. Tao, A multiple-relaxation-time lattice Boltzmann model for convection heat transfer in porous media, Int. J. Heat Mass Transf. 73 (2014) 761–775.
[34] A. Grucelski, J. Pozorski, Lattice Boltzmann simulations of heat transfer in flow past a cylinder and in simple porous media, Int. J. Heat Mass Transf. 86 (2015) 139–148.
[35] C.-Y. Zhao, L. Dai, G. Tang, Z. Qu, Z. Li, Numerical study of natural convection in porous media (metals) using lattice Boltzmann Method (LBM), Int. J. Heat Fluid Flow 31 (5) (2010) 925–934.
[36] R. Mohebbi, H. Heidari, Lattice Boltzmann simulation of fluid flow and heat transfer in a parallel-plate channel with transverse rectangular cavities, Int. J. Mod. Phys. C 28 (03) (2017) 1750042.
[37] R. Mohebbi, M. Rashidi, Numerical simulation of natural convection heat transfer of a nanofluid in an L-shaped enclosure with a heating obstacle, J. Taiwan Inst. Chem. Eng. 72 (2017) 70–84.
[38] W. Minkowycz, A. Haji-Sheikh, K. Vafai, On departure from local thermal equilibrium in porous media due to a rapidly changing heat source: the Sparrow number, Int. J. Heat Mass Transf. 42 (18) (1999) 3373–3385.
[39] Q. Zou, X. He, On pressure and velocity boundary conditions for the lattice Boltzmann BGK model, Phys. Fluids 9 (6) (1997) 1591–1598.
[40] D.A. Nield, A. Bejan, Convection in Porous Media, Springer Science & Business Media, 2006.
[41] P.D. Noymer, L.R. Glicksman, A. Devendran, Drag on a permeable cylinder in steady flow at moderate Reynolds numbers, Chem. Eng. Sci. 53 (16) (1998) 2859–2869.
[42] A.J.C. Ladd, Numerical simulations of particulate suspensions via a discretized Boltzmann equation. Part 2. Numerical results, J. Fluid Mech. 271 (1994) 311.
[43] X. He, L.-S. Luo, Theory of the lattice Boltzmann method: from the Boltzmann equation to the lattice Boltzmann equation, Phys. Rev. E 56 (6) (1997) 6811.
[44] A. Sharma, V. Eswaran, Heat and fluid flow across a square cylinder in the two-dimensional laminar flow regime, Numer. Heat Transf. Part A: Appl. 45 (3) (2004) 247–269.
[45] B. Paliwal, A. Sharma, R. Chhabra, V. Eswaran, Power law fluid flow past a square cylinder: momentum and heat transfer characteristics, Chem. Eng. Sci. 58 (23) (2003) 5315–5329.
[46] J. Lage, Effect of the convective inertia term on Bénard convection in a porous medium, Numer. Heat Transf. 22 (4) (1992) 469–485.